

AD-A253 849 GE

Form Approved
OMB No. 0704-0188

Public reporting burden
gathering and maintaining
collection of information
Data Highway, Suite 1:



response, including the time for reviewing instructions, searching existing data sources,
ormation. Send comments regarding this burden estimate or any other aspect of this
arters Services, Directorate for Information Operations and Reports, 1215 Jefferson
dget. Paperwork Reduction Project (0704-0188), Washington, DC 20503.

1. AGENCY USE ONLY (Leave blank)

2. REPORT DATE

3. REPORT TYPE AND DATES COVERED
FINAL 1 Sep 89 - 31 Jan 92

4. TITLE AND SUBTITLE
"TOMOGRAPHIC MATHEMATICAL IDEAS APPLIED TO RADAR
DETECTION" (U)

5. FUNDING NUMBERS
62301E
7090/00

6. AUTHOR(S)
Dr. Marvin Bernfeld

7. PERFORMING ORGANIZATION NAME(S) AND ADDRESS(ES)
Raytheon Company
Equipment Division
430 Boston Post Road
Wayland, MA 01778

8. PERFORMING ORGANIZATION
REPORT NUMBER
AFOSR-TR- 92 0718

9. SPONSORING / MONITORING AGENCY NAME(S) AND ADDRESS(ES)
AFOSR/NM
Bldg 410
Bolling AFB DC 20332-6448

10. SPONSORING / MONITORING
AGENCY REPORT NUMBER
F49620-89-C-0116

11. SUPPLEMENTARY NOTES

DTIC
SELECTE
S B D
JUL 29 1992

12a. DISTRIBUTION / AVAILABILITY STATEMENT
Approved for public release;
Distribution unlimited

12b. DISTRIBUTION CODE
UL

13. ABSTRACT (Maximum 200 words)

By integrating the echoed pulses after detection, a Chirp diversity radar incorporating tomographic methods possesses non of the symptoms associated with conventional pulse Doppler techniques. The point spreading is a thumbtack-like function. Thus, range-Doppler coverage is unlimited since there are no ambiguity pop-ups to restrict this coverage. In addition, it appears that the mainlobe width depends exclusively on bandwidth. In contrast, the classic thumbtack ambiguity function is affected both by bandwidth and, inversely, by the integration time. More important than the preceding discovery is the property that ambiguity function is not constrained by radar uncertainty principles. Hence, "the sands of the beach" is not a suitable analogy to describe this ambiguity function. It is concluded that this superthumbtack characteristic offers superior resolution for an accurate interpretation of radar backscatter with respect to detection, parameter estimates, and imaging.

14. SUBJECT TERMS

15. NUMBER OF PAGES
42

16. PRICE CODE

17. SECURITY CLASSIFICATION
OF REPORT
UNCLASSIFIED

18. SECURITY CLASSIFICATION
OF THIS PAGE
UNCLASSIFIED

19. SECURITY CLASSIFICATION
OF ABSTRACT
UNCLASSIFIED

20. LIMITATION OF ABSTRACT
SAR

Raytheon

**Tomographic Mathematical Ideas
Applied To Radar Detection**

**Final Technical Report
Period: November 1989 - February 1992**

Sponsored By:

**Defense Advance Research Projects Agency
DARPA Order No: 7090
AFOSR Contract: F49620-89-C-0116**

PRINCIPAL INVESTIGATOR

**Marvin Bernfeld
Raytheon Company
Equipment Division
430 Boston Post Road
Wayland, MA 01778**

92 7 27 067

92-20157


Raytheon

Tomographic Mathematical Ideas Applied To Radar Detection

Final Technical Report

Period: November 1989 - February 1992

Sponsored By:

Defense Advance Research Projects Agency

DARPA Order No: 7090

AFOSR Contract: F49620-89-C-0116

PRINCIPAL INVESTIGATOR

**Marvin Bemfeld
Raytheon Company
Equipment Division
430 Boston Post Road
Wayland, MA 01778**

The Views And Conclusions Contained In This Document Are Those Of The Authors And Should Not Be Interpreted As Necessarily Representing The Official Policies Or Endorsements, Either Expressed Or Implied, Of The Defense Advanced Research Projects Agency Or The U. S. Government.

Distribution

Copies

Dr. James M. Crowley, LtCol., USAF
Defense Advanced Research Projects Agency
Applied and Computational Mathematics Program
3701 N. Fairfax Drive Arlington , Virginia 22203-1703

2

Jerry Genello
RL/OCTS
Griffiss Air Force Base
Rome, NY 13441-5700

1

Dr. F. Alberto Grunbaum, Chairman
Mathematics Department
University of California
2939 Ashby Avenue
Berkeley, CA 94705

1

Dr. Jim Michels
RL/OCTM
Griffiss Air Force Base
Rome, NY 13441-5700

1

Dr. Arje Nachman
Air Force Office of Scientific Research
Directorate of Mathematics and Information Sciences
Building 410
Bolling Air Force Base
Washington, DC 20332-6448

6

Dr. Vincent Vannicola
RL/OCTS
Griffiss Air Force Base
Rome, NY 13441-5700

1

Accession For	
NTIS GRA&I	<input checked="" type="checkbox"/>
DTIC TAB	<input type="checkbox"/>
Unannounced	<input type="checkbox"/>
Justification	
By _____	
Distribution/	
Availability Codes	
Dist	Avail and/or Special
A-1	

DTIC QUALITY INSPECTED 2

Table of Contents

	<u>Page</u>
Distribution	i
List of Figures	iii
1.0 Preface	1
2.0 Introduction	1
3.0 Tomographic Projections in Radar	2
4.0 Investigations and Results	9
4.1 Point Spread Function	11
4.2 Aliasing Phenomena	15
4.3 Adjacent Target Detection	19
4.4 Fuzzy Projections	22
4.5 A Primitave Target Model	24
5.0 Comparison of Two Imaging Approaches	26
6.0 Computational Framework	28
7.0 Conclusion	32
8.0 References	34
Appendix A : Test and Demonstration Configuration	A1

LIST OF FIGURES

Figure		Page
1	COMPUTERIZED TOMOGRAPHY	1
2	SYSTEM GEOMETRY	2
3	A RADAR SCENARIO	3
4	CHIRP AMBIGUITY FUNCTION	6
5	RADAR-ANALOGY PROJECTIONS	7
6	AVENUES OF INVESTIGATION	9
7	THUMBTRACK AMBIGUITY FUNCTION	11
8	AMBIGUITY FUNCTION: SHIFT REGISTER SEQUENCES ...	11
9	AMBIGUITY FUNCTION: CHIRP DIVERSITY RADAR	12
10	IMPULSE RESPONSE FOR CANONIC PROJECTION FILTER ..	12
11	EXPANDED POINT SPREAD FUNCTION	13
12	POINT SPREAD FUNCTION VERSUS SAMPLING RATE	13
13	AIRY PATTERN	14
14	CHIRP DIVERSITY RADAR POINT SPREAD	15
	FUNCTIONS FOR:	
	a) 9 projections	
	b) 10 projections	
	c) 36 projections	
15	CHIRP DIVERSITY RADAR POINT SPREAD	16
	FUNCTIONS:	
	a) 32 samples	
	b) 64 samples	
	c) 128 samples	
16	EXPANDED POINT SPREAD FUNCTION	17
	FOR n PROJECTIONS: n=1,2,4,9,18,36,72	
--	(ALIASING PHENOMENA ILLUSTRATIONS)	18

(CONTINUED NEXT PAGE)

<u>Figure</u>		<u>Page</u>
17	ADJACENT TARGETS WITH DIFFERENT AMPLITUDES:	19
	a) 0 DB	
	b) -10 DB	
	c) -25 DB	
18	COMPETING TARGETS	20
19	CHIRP DIVERSITY RADAR POINT SPREAD FUNCTION WHEN PROJECTIONS ARE MISSING	21
20	CHIRP DIVERSITY RADAR IMAGE FOR TWO POINT TARGETS, WITH ONE OF THE TARGETS POSITIONED SO THAT ITS IMAGE WOULD APPEAR IN THE WEDGE-LIKE RESPONSE VOID WHICH IS CAUSED BY MISSING PROJECTIONS DURING TOMOGRAPHIC PROCESSING	21
21	POINT SPREAD FUNCTION FOR FUZZY LINE-INTEGRAL PROJECTIONS	22
22	HEMISPHERE RECONSTRUCTIONS WITH EXACT AND FUZZY LINE-INTEGRAL PROJECTIONS	23
23	A PRIMITIVE EXAMPLE OF TOMOGRAPHIC RECONSTRUCTION IN RADAR, IN WHICH A ROTATING RING-LIKE OBJECT IS THE TARGET	25
24	COHERENT DOPPLER PROCESSING:	26
	a) FFT INPUT SAMPLES	
	b) BASIC SIGNAL PROCESSING	
25	"BED OF NAILS"	26
26	A SYSTEM CONFIGURATION BASED ON TIME EXPANSION PULSE COMPRESSION	28
27	THE PROJECTION OPTIONS: $P_0(\tau)$ AND $P_0(\phi)$	29
28	A SYSTEM CONFIGURATION BASED ON FREQUENCY COMPARISON TECHNIQUE	31
A ₁	TEST AND DEMONSTRATION CONFIGURATION	A1
A ₂	TEST RANGE CONFIGURATION	A2

1.0 PREFACE

This is the final report pursuant to DARPA Order No. 7090. This report is based on a study that was conducted at Raytheon Company, Wayland, Massachusetts between November 1989 and February 1992. The subject consisted of tomographic mathematical ideas applied to radar detection. The study was monitored by the Air Force Office of Scientific Research, Bolling AFB, Washington, DC, under Contract No. F49620-89-C-0116.

The objective of DARPA Order No. 7090 was to produce a computational framework for incorporating Radon Transform techniques into radar. The particular goal is a novel radar system that can map electromagnetic backscatter as a function of range and range rate (or Doppler shift).

2.0 INTRODUCTION

The idea of reconstructing a two-dimensional distribution from corresponding line-integral projections, which are available for all aspect angles distributed over 180 degrees, was introduced in 1917 by Johann Radon. These mathematical results have since inspired developments in diverse fields.

The best known is in clinical radiology where it is referred to as Computerized Tomography (or CT). Tomo in Greek means slice (see fig. 1). The value of CT is an ability to routinely produce x-ray images of pathologically interesting cross-sections that are normally inaccessible such as illustrated in figure 1, without destructive surgery.

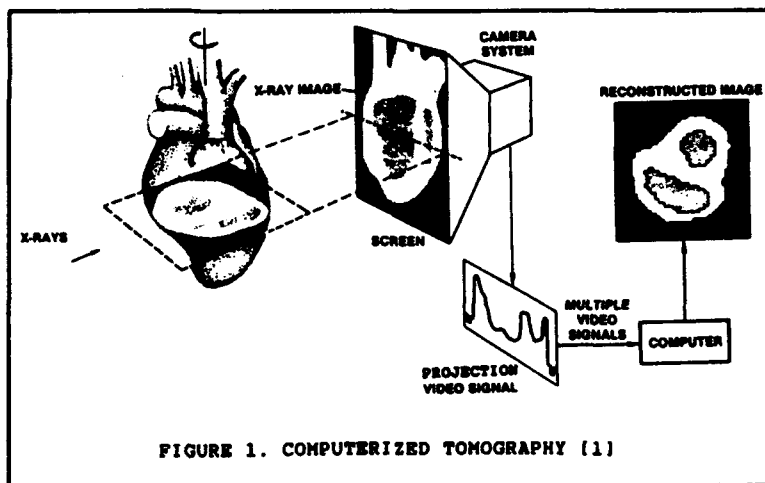


FIGURE 1. COMPUTERIZED TOMOGRAPHY [1]

Radar astronomy, geophysical probing, and non-destructive testing at industrial laboratories are some other fields where this idea has also been successfully exploited [2-5]. Moreover, the principles are not unfamiliar to radar engineers who have perceived that synthetic aperture techniques (SAR) as well as ISAR imaging are based on projections similar to Radon's line-integral projections [6,7].

Johann Radon's mathematical method for reconstructing two-dimensional distributions was recently adopted yet another time [8,9]. This time the application is to reconstruct distributions of radar backscatter intensity as a function of range delay and Doppler shift (or range and range-rate). The basis for this

innovation in radar imaging technology is that analogous line-integral projections can be obtained for these distributions by viewing targets with a matched filter radar system incorporating a suite of linear FM pulses which vary in their Chirp slope. This application stands alone among the applications of tomographic methods since the projection angles are controlled electronically in contrast with mechanical steering that is required in all the other cases.

3.0 TOMOGRAPHIC PROJECTIONS IN RADAR

The procedure in modern radiology for imaging pathologically interesting cross-sections, based on some distribution of x-ray attenuation, denoted by $g(r, \psi)$, is founded on the inversion of its tomographic projections. The classic inversion formula, which was derived by Johann Radon is

$$g(r, \psi) = \frac{1}{4\pi^2} \int_0^\pi d\theta \int_{-\infty}^{\infty} dx' \frac{\partial p(x', \theta) / \partial x'}{r \cos(\psi - \theta) - x'} \quad (1)$$

where the variables x , x' , y , r , θ , and ψ are identified in figure 2 and the tomographic projections are denoted by $p(x', \theta)$. The latter can be represented mathematically by the following line-integrations.

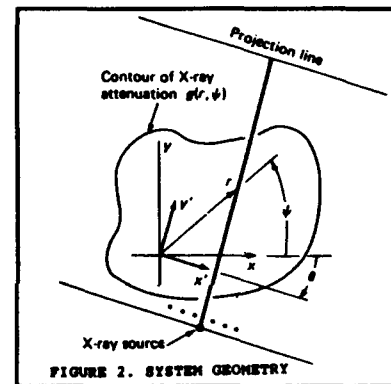


FIGURE 2. SYSTEM GEOMETRY

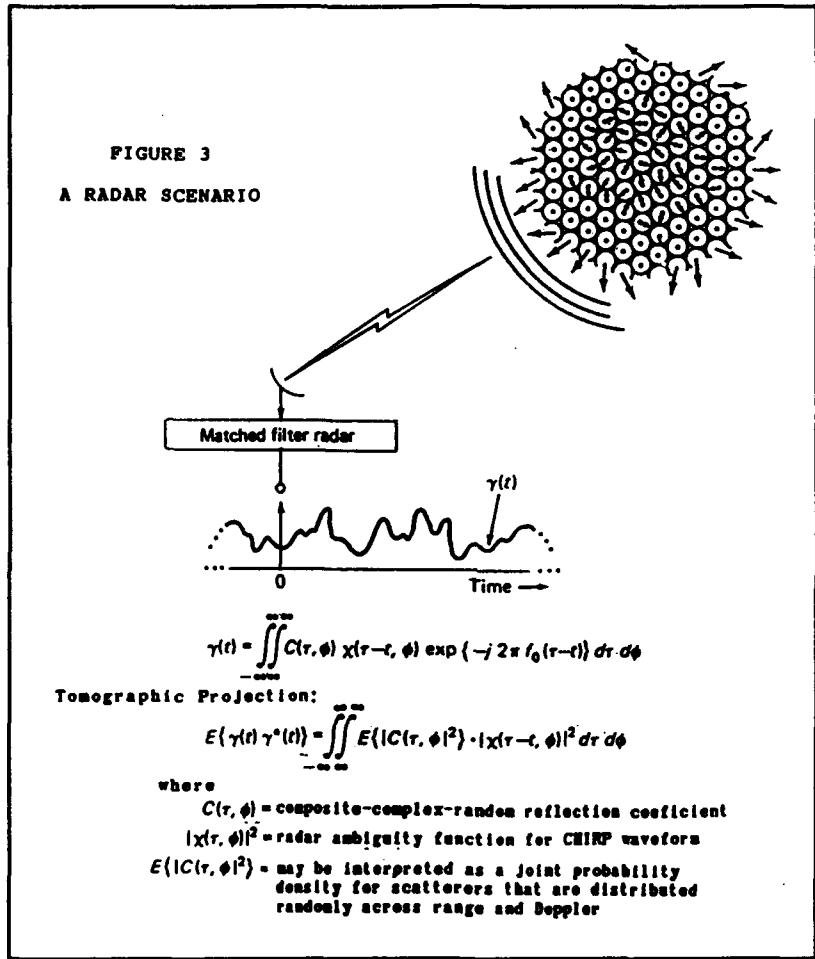
$$p(x', \theta) = \int_{-\infty}^{\infty} \int_{-\infty}^{\infty} f(x, y) \delta(x' - (x \cos\theta - y \sin\theta)) dx dy \quad (2)$$

where $f(x, y) = g(r, \psi)$ and $\delta()$ denotes a line-type δ -function.

The second equation is also the description for two-dimensional Radon Transforms. Thus, this describes the transformation from some two-dimensional distribution to a set of the one-dimensional line-integral projections. In medical imaging, these tomographic projections, such as they are called, are comprised of discrete samples of the total x-ray attenuation across a slice of interesting pathology. The classic configuration consists of penetrating x-rays that are parallel and equally spaced so that there will be appropriate linear sampling of the cross-section. Regarding individual projections, the paths traversed by the x-rays are defined by $x' = x \cos\theta - y \sin\theta$, where θ denotes the angle of penetration; this is held constant while the individual projection is being constructed. Repeating such constructions, for a sequence

of mechanical realignments providing appropriate sampling over 180° , yields the projections that are transformed into an image of the original x-ray attenuation distribution.

For radar imaging, tomographic projections can be obtained by transmitting a suite of linear FM pulses. To explain this idea, the backscatter generated by one of these pulses and intercepted by a matched filter, as illustrated in figure 3, is depicted as a composite echo corresponding to a dispersal of point scatterers whose ranges and range rates are distributed in some random way.



In this particular model, the scattering scenario can be represented by a statistical reduction of the composite echo amplitudes (C) distributed over range and range rate. Thus, expressed in terms of range delay (τ) and (for the narrowband case) in terms of Doppler shift (ϕ), an appropriate representation for the scattering scenario is the scattering function

$$s(\tau, \phi) = E\{|C(\tau, \phi)|^2\} \quad (3)$$

where $E\{\dots\}$ is utilized to denote the statistical expected value.

The scattering function will also change with time, but the variations will normally be relatively narrowband with respect to the dwell that is required to obtain sufficient projections. For the case of uniform individual scattering cross-sections " the scattering function has all the properties of a joint probability density".

The scattering function is the radar analog with respect to the distribution of x-ray attenuation in medical imaging. The following provides the basis for obtaining tomographic projections with a suite of linear FM pulses.

The composite backscatter described above can be expressed mathematically as follows

$$\zeta(t) = \iint C(\tau, \phi) \Psi(t+\tau, \phi) d\tau d\phi \quad (4)$$

where $\Psi(t, \phi)$ denotes the complex notation for transmission signals displaced with respect to the carrier f_0 by ϕ Doppler shift. The classic criteria for the narrowband approximation of the Doppler effect is that time-bandwidth product must be smaller than half the velocity ratio c/v where c and v denote light and range-rate velocities, respectively. This condition is almost always met by radar systems in operation today.

A matched filter that conforms with respect to the description of the transmitted waveform will yield the following response corresponding to (4).

$$\begin{aligned} \gamma(t) &= \int \zeta(v) \Psi^*(t+v) dv \\ &= \iiint C(\tau, \phi) \Psi(t+v, \phi) \Psi^*(t+v) dv d\tau d\phi \end{aligned} \quad (5)$$

By substituting $v+\tau=\epsilon$, (5) can be rewritten as follows.

$$\gamma(t) = \iint C(\tau, \phi) \left[\int \Psi(\epsilon, \phi) \Psi^*(t-\tau+\epsilon) d\epsilon \right] d\tau d\phi \quad (6)$$

If $\mu(t)$ is the complex pre-envelope modulation superimposed on transmissions of a carrier f_0 , then

$$\begin{aligned} \Psi(\epsilon, \phi) &= \mu(\epsilon) \exp[j2\pi(f_0 + \phi)\epsilon] \\ \Psi^*(t-\tau+\epsilon) &= \mu^*(t-\tau+\epsilon) \exp[-j2\pi(f_0 + \phi)(t-\tau+\epsilon)] \end{aligned}$$

An equivalent mathematical representation for (6) can now be derived by introducing Woodward's two-dimensional correlation function.

$$\chi(\tau, \phi) = \int_{-\infty}^{\infty} \mu(t) \mu^*(t+\tau) \exp(j2\pi\phi t) dt \quad (7)$$

Thus, it is possible to finally express the matched filter output as follows.

$$\gamma(t) = \iint_{-\infty}^{\infty} C(\tau, \phi) \chi(\tau-t, \phi) \exp(-j2\pi f_0(\tau-t)) d\tau d\phi \quad (8)$$

Based on the stochastic model that was adopted above for the backscatter amplitudes, this matched filter output represents a stochastic process. This can be reduced by invoking the following ensemble averaging.

$$E\{|\gamma(t)|^2\} = \iint_{-\infty}^{\infty} E\{|C(\tau, \phi)|^2\} |\chi(\tau-t, \phi)|^2 d\tau d\phi \quad (9)$$

where $|\chi(\tau, \phi)|^2$ denotes the radar ambiguity function.

The similarity of equation (9) with medical-imaging projections can be revealed by examining the ambiguity function for linear FM (LFM). The characteristic ambiguity function, with respect to linear FM pulses, has the appearance of a ridge-like surface with an alignment which coincides with $v\tau - \phi = 0$ where v , the slope of this line, is equal to the LFM (or, Chirp) rate. (Note that the symbol v was previously used in this document with a different identity.)

The following ambiguity function properties provide another perspective of the relationship between the direction of this ridge and the Chirp rate.

PROPERTY I

IF: $\mu(t) \rightsquigarrow \chi(\tau, \phi)$

THEN: $\mu(t) \exp(jat^2) \rightsquigarrow \chi(\tau, \phi - \frac{a\tau}{\pi})$

PROPERTY II

IF: $U(f) = \mathcal{F}\{\mu(t)\}$

THEN: $U(f) \exp(jhf^2) \rightsquigarrow \chi(\tau + \frac{h\phi}{\pi}, \phi)$

In particular, for pulsed LFM

$$\mu(t) = \sqrt{\frac{1}{T}} \exp(j\pi\nu t^2) \quad ; |t| \leq \frac{T}{2} \quad (10)$$

$$|\chi(\tau, \phi)| = (1 - \frac{|\tau|}{T})$$

$$\frac{\sin\pi[\nu\tau - \phi][T - |\tau|]}{\pi[\nu\tau - \phi][T - |\tau|]} \quad ; |\tau| \leq T \quad (11)$$

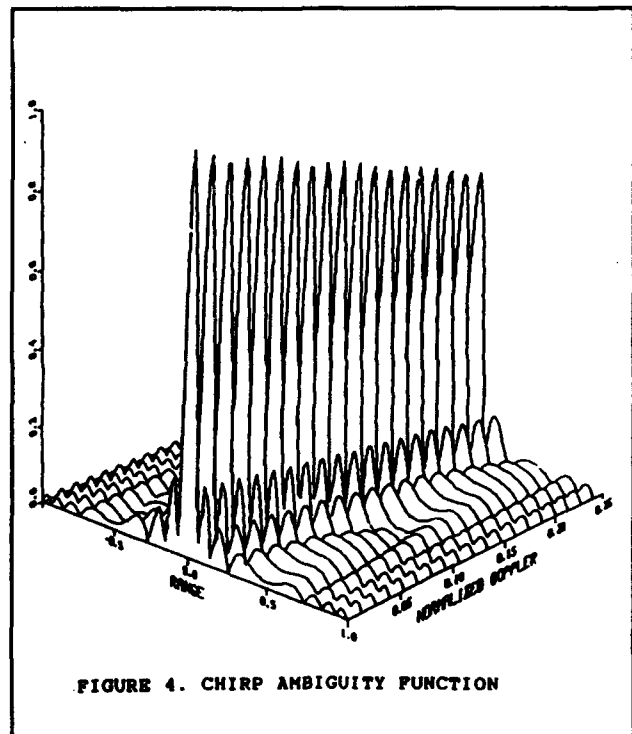


FIGURE 4. CHIRP AMBIGUITY FUNCTION

Figure 4 provides a specific example of the ambiguity function associated with Chirp pulse compression, computed for a time duration (T)-swept bandwidth (Δf) product of 15. Only the upper

right quadrant of (11) is displayed. Since the base coordinates τ and ϕ are normalized in this figure, with respect T and Δf , respectively, the ridge line may appear to have unity slope but actually the slope can be anything depending on how the product $T\Delta f$ is factored into a ratio.

For pulses with sufficiently large bandwidth, the ridge will be sufficiently sharp that $|\chi(\tau, \phi)|^2$ can be approximated by the line-type δ -function, so that (9) reduces to the output

$$f(t, \beta) = \iint E\{|C(\tau, \phi)|^2\} \delta(t - (\tau + \frac{\phi}{v})) d\tau d\phi \quad (12)$$

where $\beta = \arctan\{v\}$. Some interesting projection options are presented in Section 6 of this report.

The illustration in figure 5. will be helpful regarding an interpretation of (12). The ambiguity function is depicted in this figure as a v -tilted window that travels laterally across the $\tau\phi$ -plane parallel to the τ axis. The total scattering power overlaid by this window is effectively accumulated at every lateral position as a function of time. Thus, this output may be interpreted as a tomographic projection of the scattering function, therefore it can be combined with other such projections according to the inversion formula given by equation 1. However, to account for the relationship $t = x'/\sin \beta$, equation 1 must be amended as follows.

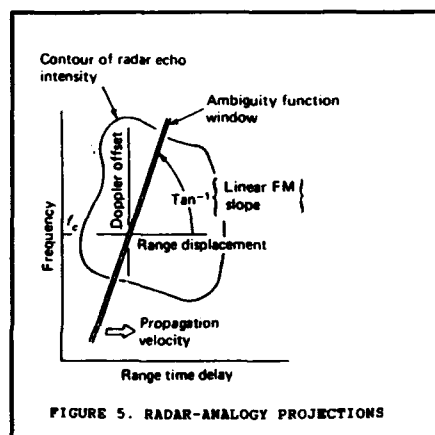


FIGURE 5. RADAR-ANALOGY PROJECTIONS

$$g(r, \psi) = \frac{1}{4\pi^2} \int_{-\frac{\pi}{2}}^{\frac{\pi}{2}} d\beta \int_{-\infty}^{\infty} dt \frac{\partial f(t, \beta) / \partial t}{r \sin(\psi - \beta) - t \sin \beta} \quad (13)$$

where $g(r, \psi) = s(\tau, \phi)$.

The projections that are combined according to (13) can be obtained by transmitting a suite of linear FM pulses which vary in their Chirp rate; the suite size is one of the issues discussed in the next section. Since different perspectives of the scattering function are provided by changing the Chirp rate, this application of tomography differs from other applications in which mechanical rotation techniques are necessary.

Commenting on the stochastic backscatter model that was chosen for the derivation above, this model was adopted because it provided an analogy in radar for imaging with tomographic methods. All extended

targets, which consist of dense scattering points that are physically disturbed by some random process, are represented by this model. Some examples are (1), the ionized wake attached to a reentry vehicle, (2), ionospheric frequency versus altitude profiles, (3), microburst turbulence over airport runways, (4), rain clouds, (5), radar clutter from foliage, and (6), rough-surfaced rotating objects. The stochastic model, therefore, is not regarded as very restrictive in finding specific radar applications. However, another model could have been adopted which possibly is best characterized by the phrase "what you see is what you get". The proverbial point target, for example, is represented by this model. The model can also be applied to represent several isolated scattering objects. In fact, it may be applied for any target scenario which is to be imaged by snapshot measurements; even dense backscattering falls in this class. In this case, the projections of $C(\tau, \phi)$ or $|C(\tau, \phi)|^2$ available directly from the output of the matched filter do not represent a stochastic process and so are not reducible by ensemble averaging. A question arises: Is it necessary to amend the inverse Radon transform for this case? One way to find out is to engage in controlled experiments with live $C(\tau, \phi)$ distributions.

4.0 INVESTIGATIONS AND RESULTS

To prove the concept behind this novel application in radar imaging of tomographic mathematical ideas, the investigation plan (figure 6) contains several avenues that can be taken to produce and process experimental tomographic projections. This includes various computational paths for producing pre-formulated tomographic projections, two-dimensional radar distribution modeling as well as echo simulations and real backscatter demonstrations with different degrees of experimental control.

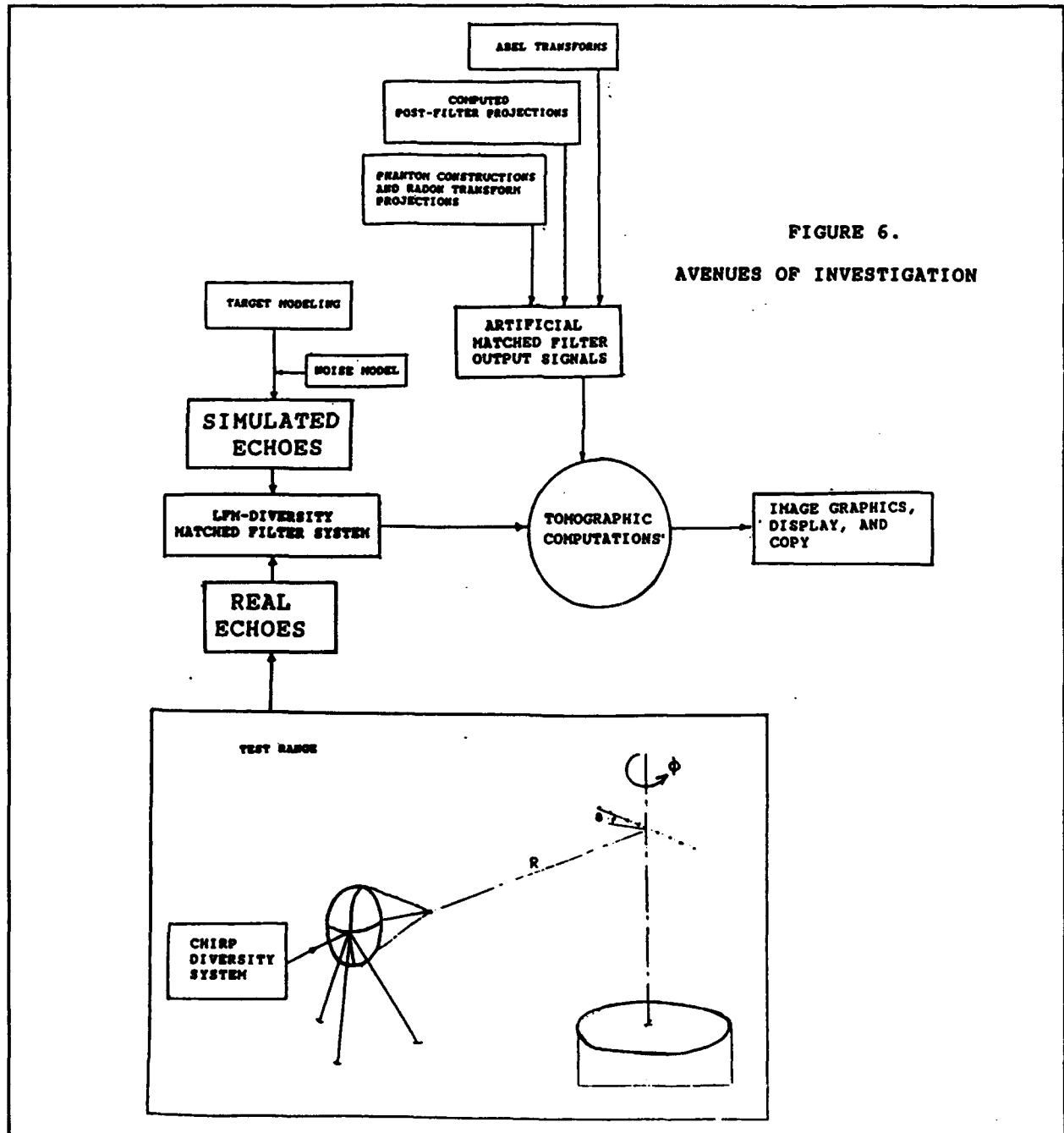


FIGURE 6.
AVENUES OF INVESTIGATION

The discussion in this section concerns the conduct of this investigation during the first phase which consisted exclusively of computational procedures involving pre-formulated and computed projections representing post match filter responses obtained with different Chirp rates. Several issues are addressed and various results are documented. In particular, the following things are discussed in this section.

- (1) The point spreading characteristic,
- (2) Parametric sensitivities,
- (3) Adjacent target detection,
- (4) Incomplete projection data,
- (5) The Radon transform approximation.

During the second phase in this investigation, which is already in stages of implementation, the plan is to simulate and process pre-match filter signals contaminated by noise. The implementation for this phase will incorporate provisions, also, for an investigation concerning

- (1) the paradoxical moving object,
- (2) coherent versus noncoherent tomographic imaging.

The third and the last phase planned for this proof-of-concept program is test and demonstration. The conduct of this phase will provide controlled experimental results for real objects. One of the system configurations described in Section 6 can be employed as the basis for supporting hardware. This phase would have to be accomplished as a follow-on of the present work. Several engineering tasks are required, including

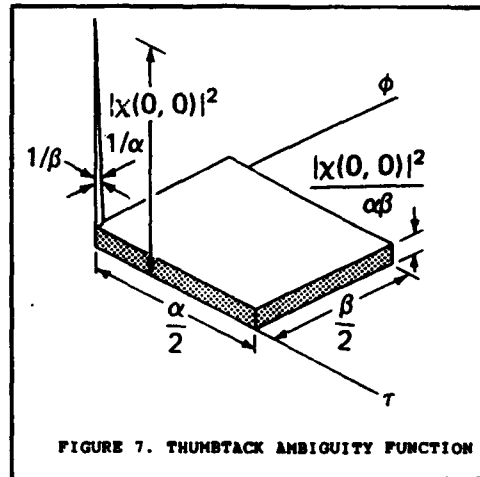
- (1) system/parameter trade-offs,
- (2) test configuration trade-offs,
- (3) hardware-software developments,
- (4) test configuration integration.

Initially, the demonstrations can be conducted with point-like object configurations consisting of one or more targets of opportunity. The purpose for this step is to confirm the basic imaging capability, offered by tomographic methods. The next step can be driven by a more ambitious goal consisting of quantifying the ability to produce accurate range and Doppler estimates. This will require greater control of the test configuration. Possible approaches are (1), calibration by another radar, (2), command-control, and (3), a controllable platform, such as a rotating disc-type surface, impregnated with scatterers. The ultimate step will be to demonstrate high resolution imaging and to compare the results with conventional pulse Doppler images. An expansion of the follow-on plan in terms of greater detail is currently being developed. Some preliminary details are provided in Appendix A.

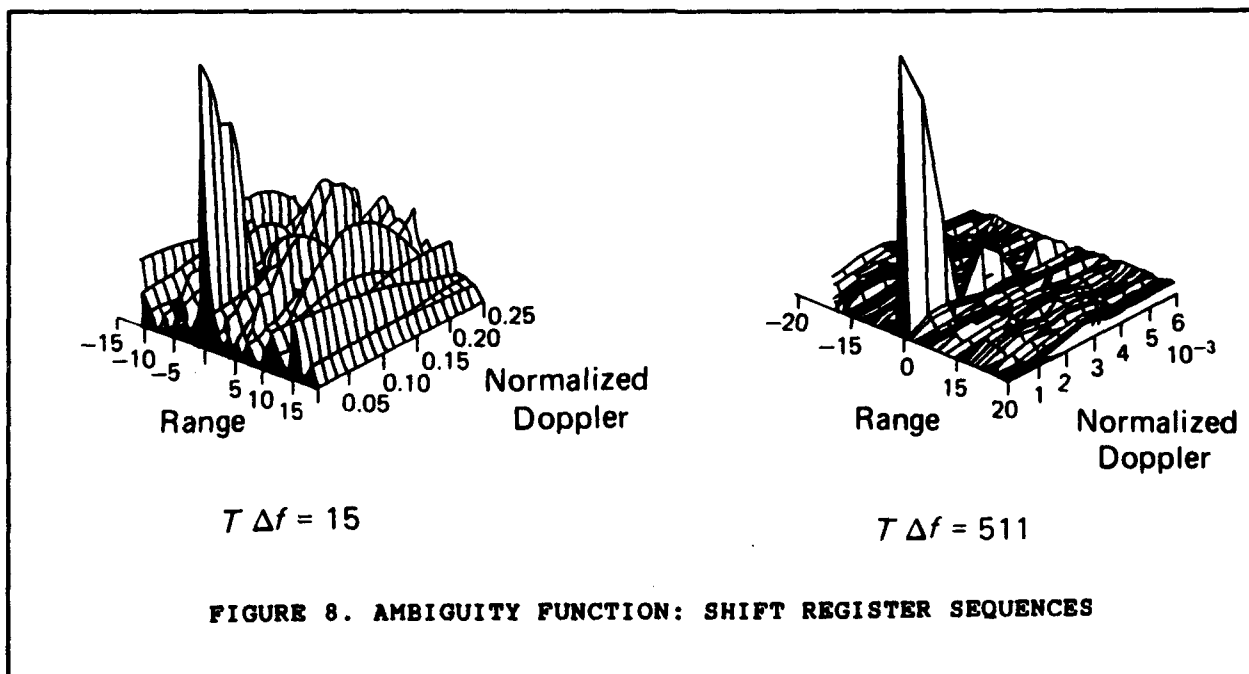
4.1 THE POINT SPREADING CHARACTERISTIC

The point-spread characteristic and the radar ambiguity function are interchangeable in the context of the following discussion.

The radar ambiguity function was introduced shortly after WW II by P.M. Woodward in his famous monograph published in 1953 [10]. Almost from the start systems engineer were dedicated to minimizing joint detection ambiguities, maximizing joint parameter estimation accuracy, and maximizing resolution and quality imaging [11]. An endless search began for optimum match-filter waveforms to employ in given situations, and radar scientists were forever intrigued by the thumbtack-like ambiguity characteristics (figure 7). Due to a fundamental constraint that restricts the ambiguity function volume to equal normalized waveform energy, the thumbtack ambiguity function has frequently been an ultimate objective in this search.



Although the waveform that can be characterized by its thumbtack ambiguity function has never been found, certain large time-bandwidth waveforms have been discovered that qualify approximately. The shift-register sequences, for example, supply a code group that has been a popular source for discrete phase modulation, yielding an rms sidelobe level that, averaged over all codes in the group, equals approximately one over the square root of time-bandwidth product. Figure 8 displays the ambiguity functions that were derived for two of these waveforms.



By applying tomographic methods, a composite ambiguity function has been derived that possess the closest known resemblance so far of the elusive thumbtack. This is presented in figure 9 which was derived by assuming a point distribution at the origin and performing the reconstruction on a 128x128 imaging palet with the projections for a suite of 36 linear FM pulses. The projections consisted of the discete samples of

$$p(u) = 2 \left[\frac{\cos u - 1}{u^2} + \frac{\sin u}{u} \right]$$

$$; u = \pi \nabla f x \quad (14)$$

where ∇f denotes bandwidth (see figure 10). This function defines the impulse response for an even symmetric ramp filter whose bandwidth is ∇f . The samples were evaluate at $x=k/\nabla f$, $k=1,2,3,etc, so they represent Nyquist sampling. Equivalent sampling intervals are employed in medical imaging during conventional tomographic processing.$

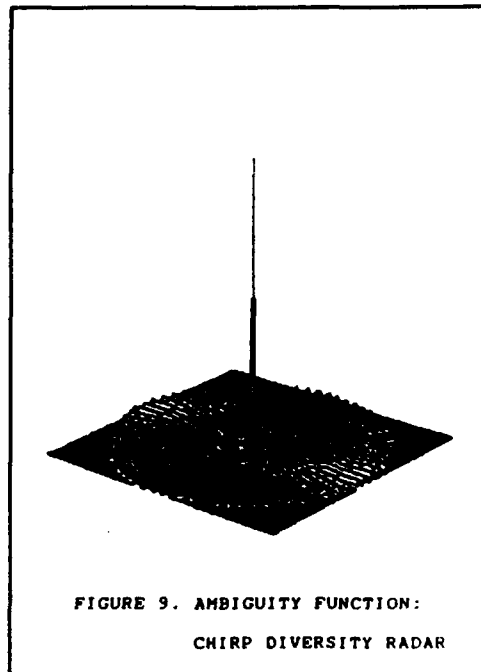


FIGURE 9. AMBIGUITY FUNCTION:
CHIRP DIVERSITY RADAR

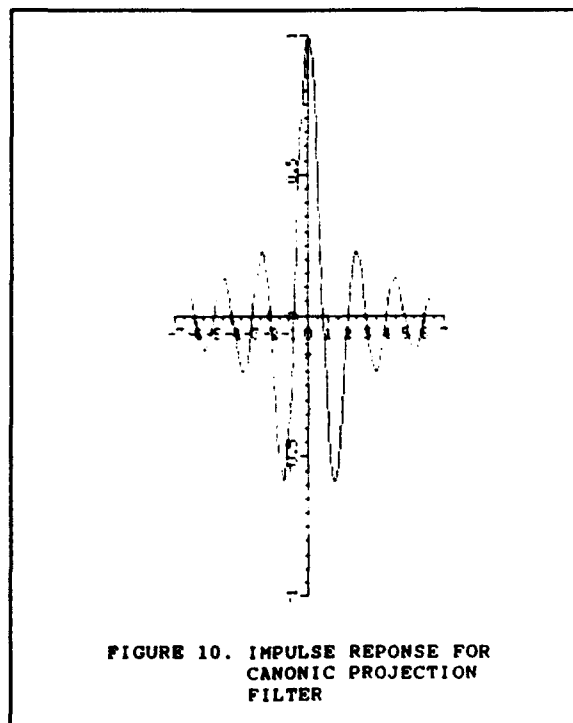
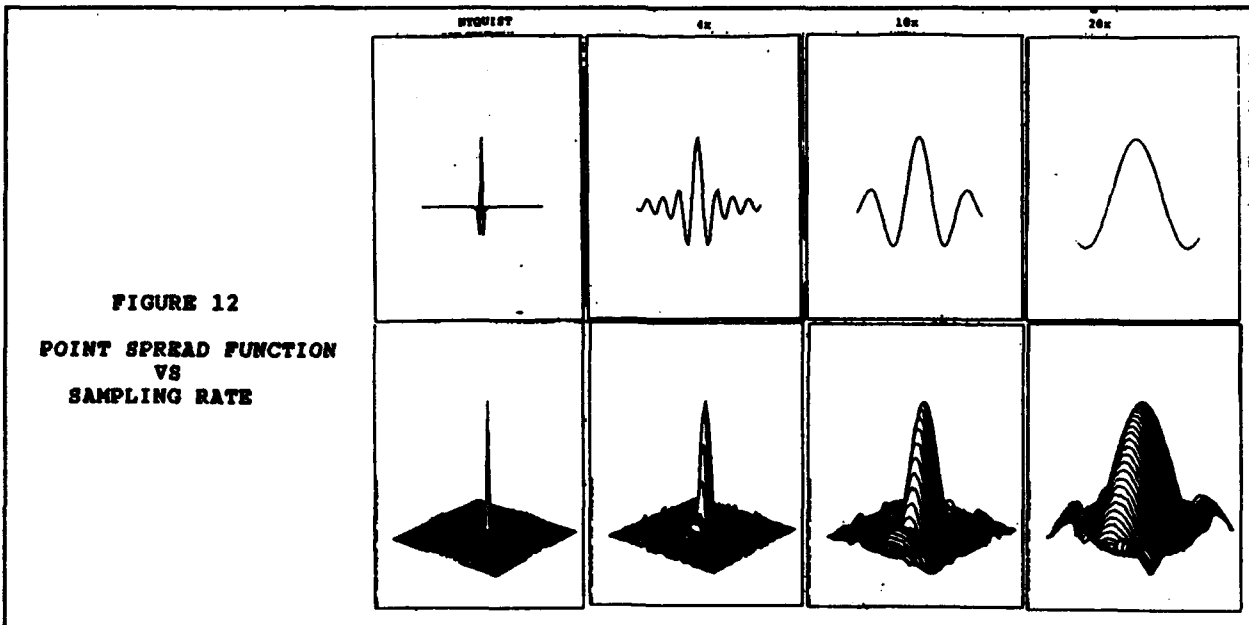
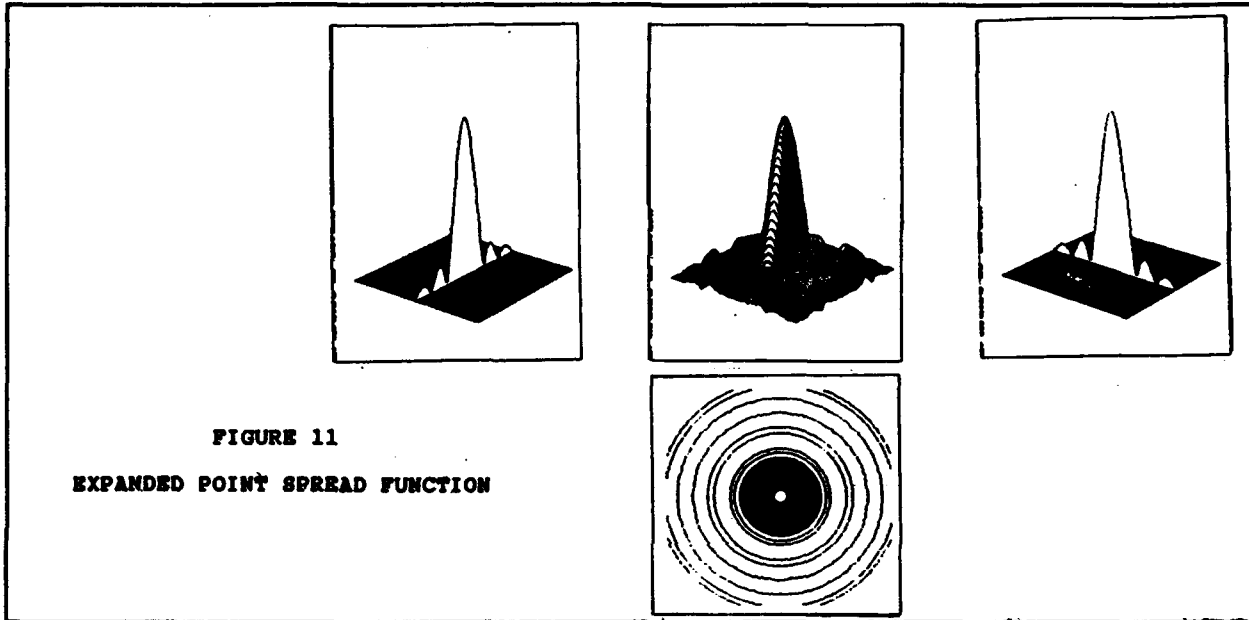


FIGURE 10. IMPULSE REPNSE FOR
CANONIC PROJECTION
FILTER

It is possible to increase the resolution of the point spread function by sampling (14) at higher than the Nyquist rate. The effect on the point spread function is illustrated in figure 11, and several specific cases showing the increased sampling density are also presented in figure 12. Positioned above each point spread function in figure 12 is its corresponding bandwidth-limited (Chirp Diversity Radar) projection; linear interpolation was employed to interconnect the discrete samples. The telescopic-like changes that are conspicuous, as the resolution is increased, can be explained by noting that equal image dimensions were employed for everyone of these cases.

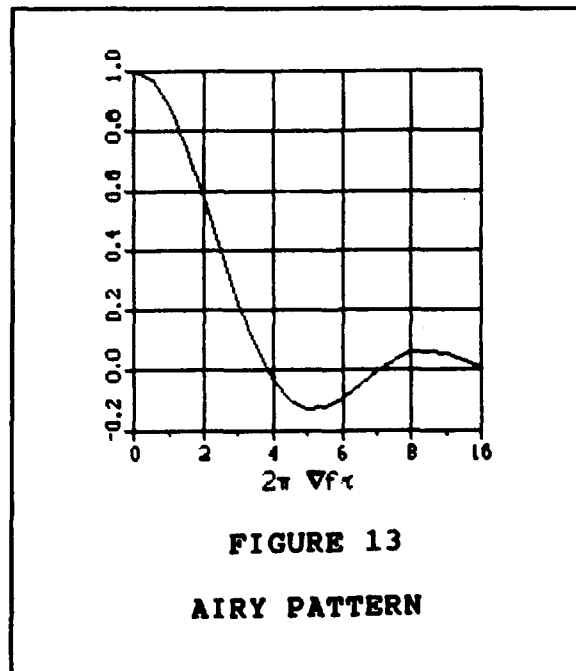


The analog form of the point spread function is revealed when the resolution becomes infinite. This is equivalent to Airy's celebrated mathematical description for Fraunhofer diffraction associated with circular apertures.

$$f(r) = 2 \frac{J_1(r)}{r} ; \quad r = 2\pi \nabla f \tau \quad (15)$$

where $J_1(\dots)$ denotes the first order Bessel function.

The Airy pattern is plotted in figure 13, revealing potentially greater point target resolution compared to the resolution that is achieved with a conventional Chirp pulse compression system. The improvement factor is approximately 2π based on the mainlobe widths measured at the base. Another discovery is that this composite ambiguity function is not constrained by uncertainty principles. Hence, "the sands of the beach" is not a suitable analogy to describe the ambiguity function. Most important, however, the composite ambiguity function is not affected by the reciprocal relationship between time and frequency since the mainlobe width on this is exclusively a function of the bandwidth. It is concluded, therefore, that by employing tomography super resolution of radar backscatter is finally within reach.

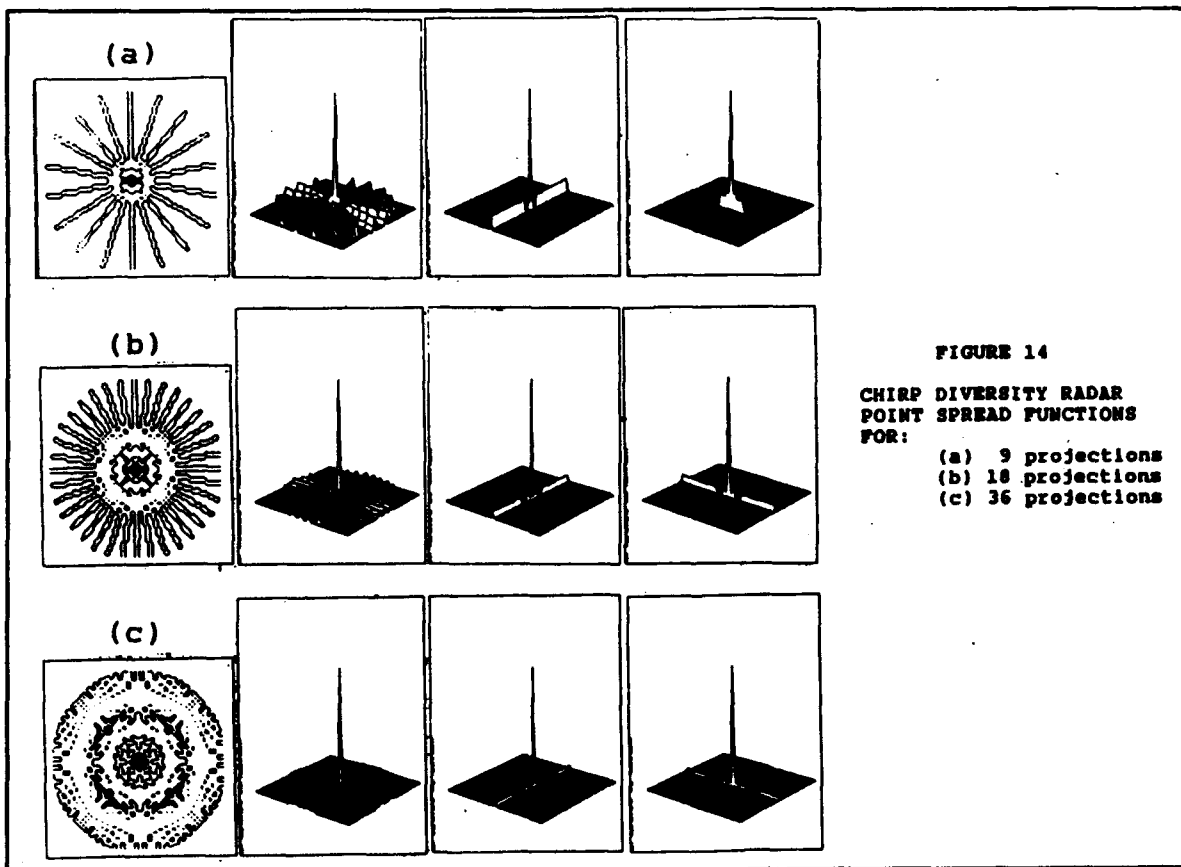


4.2 THE ALIASING PHENOMENA

The aliasing phenomena in computed tomography has previously been investigated and discussed by several authors. A list of some of these works can be found in the bibliography provided by S.R. Dean [13]. It was decided to revisit this subject since it reveals certain considerations affecting the selection of system parameters. It is believed that the investigations discussed below will provide some new perspectives on this subject.

Functionally, the AIRY pattern and the (tomography) ambiguity function depart at some point, depending on the number of projections that are employed during tomographic computations. Figure 14 depicts three results for which a different number of tomographic projections was employed. These tomographic constructions consist of 64×64 points and the number of projections corresponding to cases a, b, and c consist of 9, 18, and 36, respectively. (The constructions that are displayed in figure 14 were computed based on the same number of Nyquist samples on a projection as the rectangular dimension of the construction).

Two distinct regions are visible in each of the three constructions that are displayed. The demarcation between these regions consists of the onset of ray-like contour lines, an aliasing phenomena that has been characterized as "streaking" in the literature [14]. The

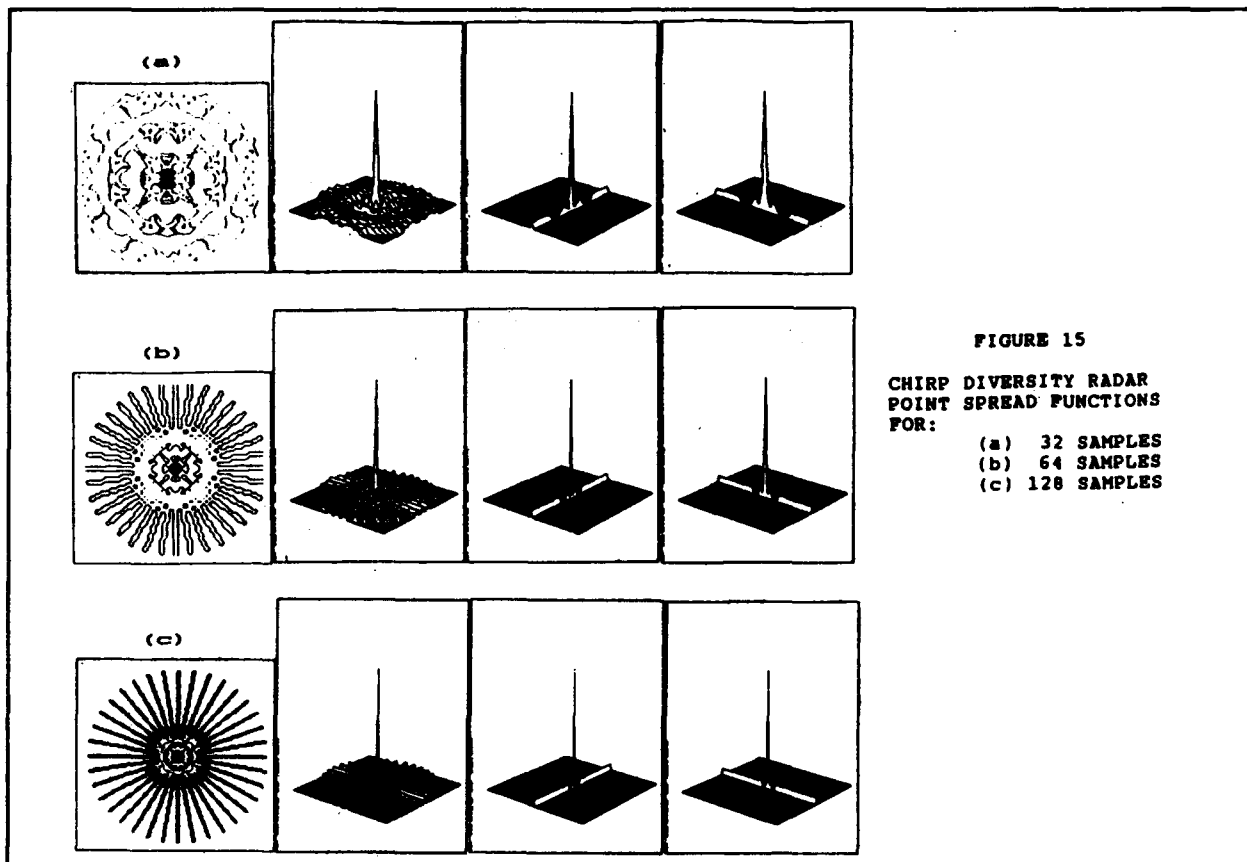


radius of the demarcation depends upon how many tomographic

projections are employed, and the functional variations out to this radius can probably be shown to conform with the AIRY pattern. The streaks have a relative amplitude, compared to the peak, that approximately equals the reciprocal of the projections. The step in amplitude at the demarcation arises since the decreasing sidelobes of the AIRY pattern are usually much smaller at the demarcation.

One puzzling fact is that the radius of the demarcation in figure 14c approximately equals one half the rectangular dimension of this image. This appears to contradict a prediction that was previously reported in the literature. It states that artifacts due to aliasing can be avoided if the number of projections is equal $\pi/2$ times the rectangular dimension on which an image is constructed. No explanation can be given at this time for this discrepancy.

Some additional results that were derived regarding this subject are presented in figures 15 and 16. Figure 15 shows several tomographic constructions that were derived with 32, 64, and 128 Nyquist samples but 18 projections in each case. Figure 16 depicts, for the case of high density sampling which was 10x the Nyquist rate, how tomographic constructions are effected when the number of projections is varied. The figure contains the tomographic constructions that were derived with 1, 2, 4, 9, 18, 36, and 72 projections employing 128 samples in each case.



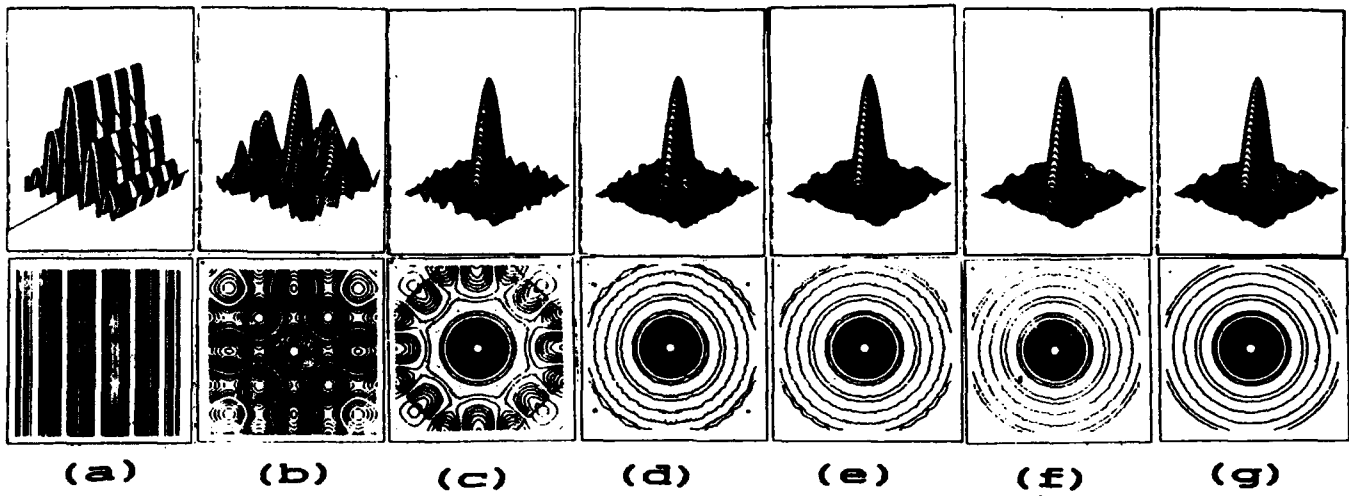
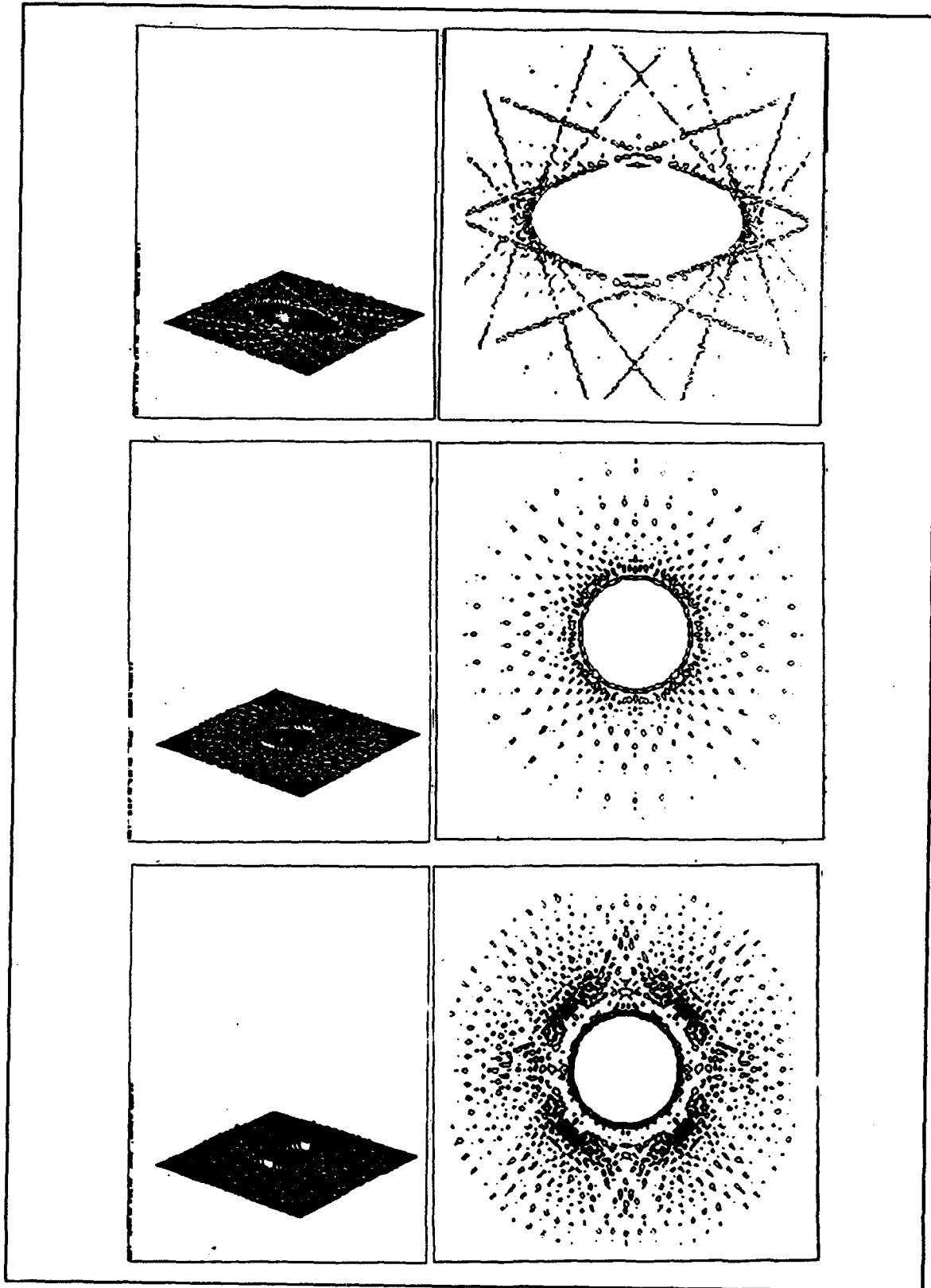


FIGURE 16
EXPANDED POINT SPREAD FUNCTIONS
FOR n PROJECTIONS:

- (a) $n = 1$
- (b) $n = 2$
- (c) $n = 4$
- (d) $n = 9$
- (e) $n = 18$
- (f) $n = 36$
- (g) $n = 72$

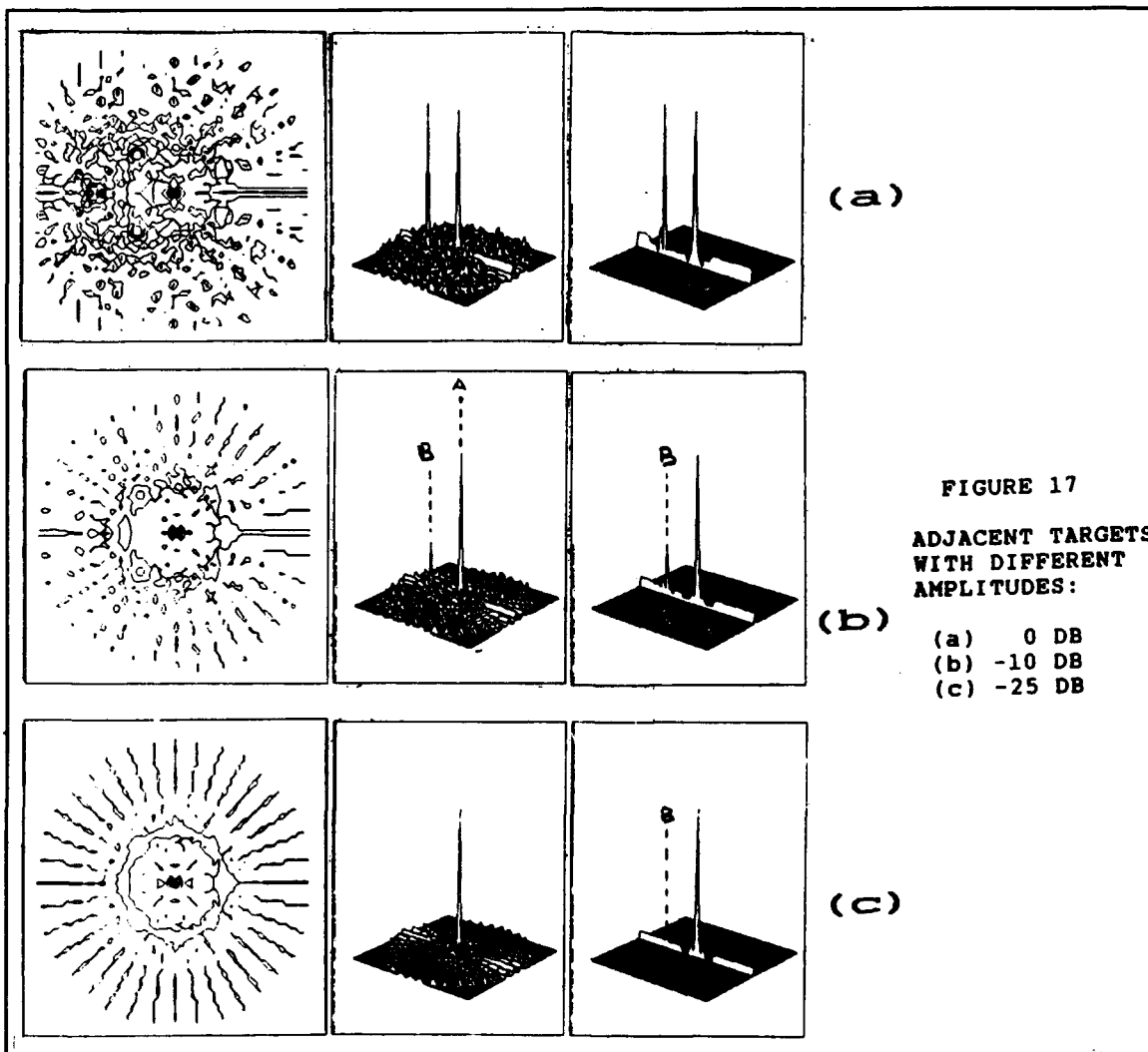
The illustrations below provide additional examples of streaking. The ellipse is constructed on 128x128 points with 18 projections. Both circle constructions also consist of 128x128 points. However, the first circle was constructed with 18 projections and the second circle with 36 projections.



4.3 ADJACENT TARGET DETECTIONS

The tomographic images for adjacent point targets, denoted by A and B, are shown in figure 17. These target were positioned sufficiently apart so as to put their images in a neighbor's aliasing artifacts. The amplitudes of target B, corresponding to a,b, and c, respectively, consist of 0, -13DB and -25DB. These results were derived by employing tomographic projections ^{that were} spaced ¹⁰⁰ apart and were comprised of 64 line-integrations. The relative amplitude of the streaking due to aliasing is slightly below -25DB. With no noise added to interfere with the detections, target B clearly is perceivable at -25 DB.

For figure 18, target B was moved in closer to target A so as to put both images in regions unaffected by aliasing. Two situations are presented in figure 18, each representing a different distances between the targets. In each case, target B has an amplitude that is equal to -25DB and is competing with AIRY sidelobes.



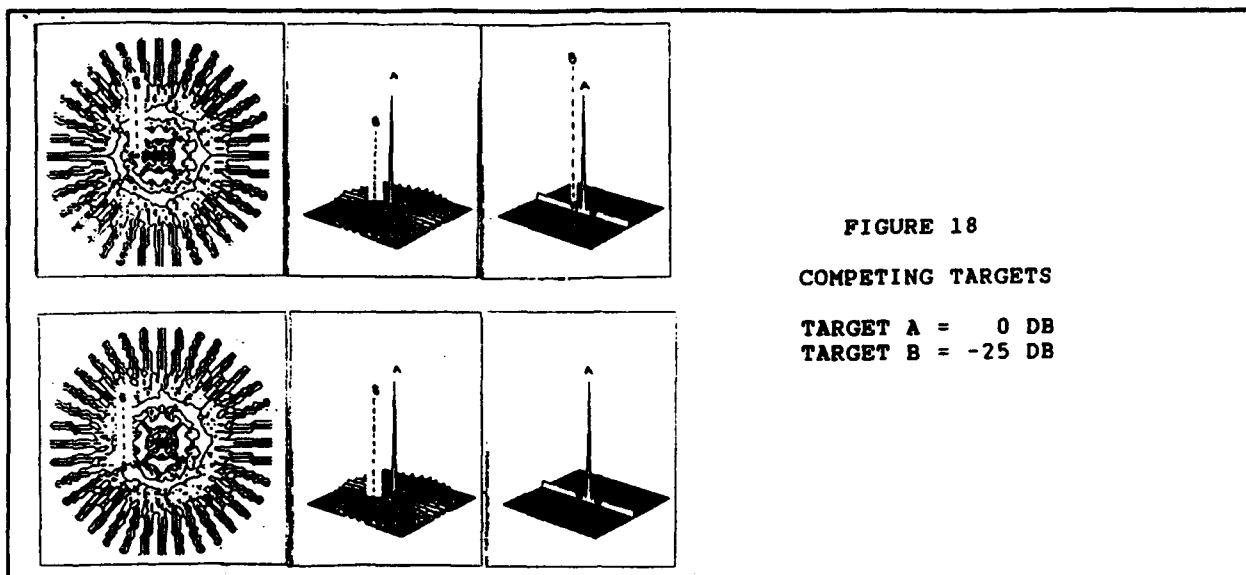


Figure 19 displays a point target image with certain projections omitted. In particular, it presents two cases where projections were omitted from a 20° sector around 0° . A condition such as this can actually arise in practice, since it may not always be practical to generate Chirp pulses that will yield valid radar-analogous tomographic projections within narrow sectors around the range delay τ axis. Similarly, but for a different practical reason, narrow sectors around the Doppler axis ϕ may also present a problem. In this case, it may not be practical to generate the high speed linear FM that is required to provide projections near 90° . However, a short time duration, CW pulse is an alternative, in lieu of an infinite linear FM rate, that can be employed to obtain the projection at 90° .

The two cases presented in figure 19 represent (a) projections separated by 5° with Nyquist sampling that yielded 128 samples, (b) projections separated by 10° with Nyquist sampling that yielded 64 samples. Figure 20 illustrates what happens to the image of two point targets, with one target positioned so that its image would appear in the wedge-like response void which is caused by missing projection during tomographic processing.

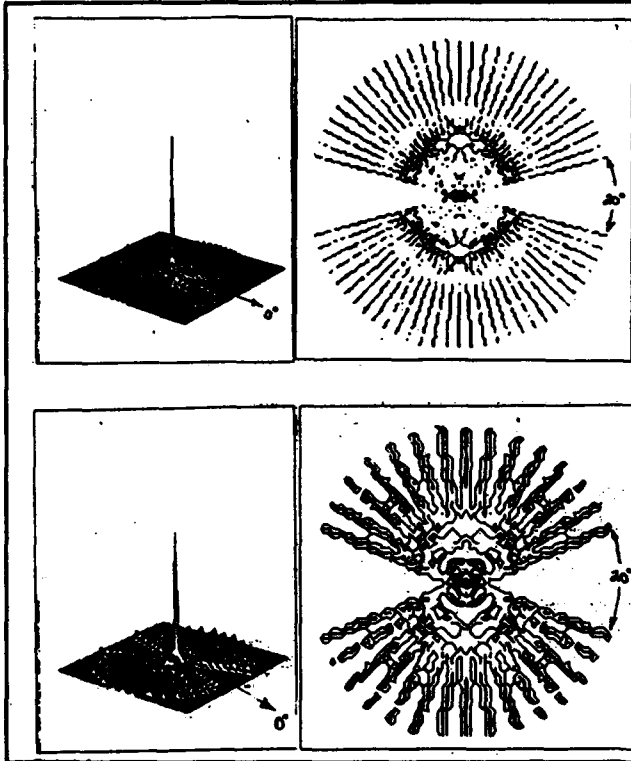


FIGURE 19

CHIRP DIVERSITY RADAR POINT SPREAD FUNCTION WHEN PROJECTIONS ARE OMITTED.

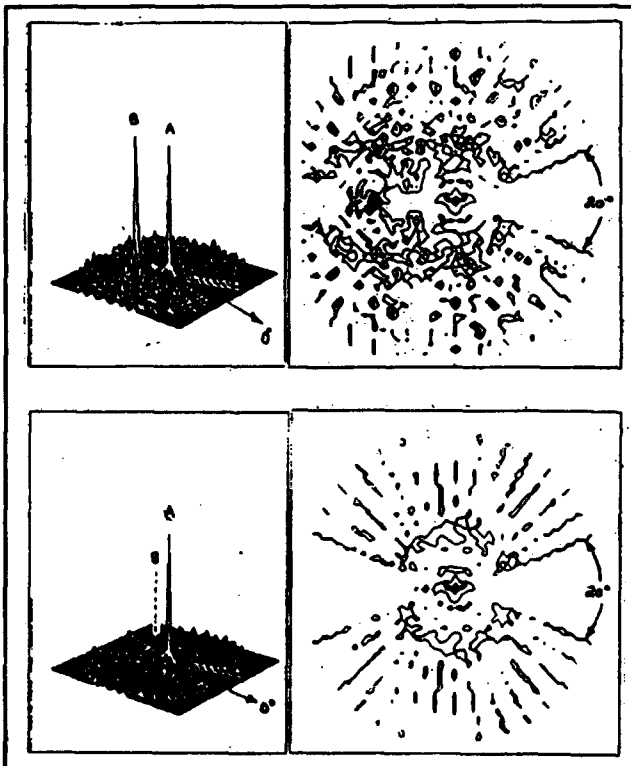


FIGURE 20

CHIRP DIVERSITY RADAR IMAGE FOR TWO POINT TARGETS, WITH ONE OF TARGET POSITIONED SO ITS IMAGE WOULD APPEAR IN THE WEDGE-LIKE RESPONSE VOID WHICH IS CAUSED BY MISSING PROJECTIONS DURING TOMOGRAPHIC PROCESSING.

4.4 FUZZY PROJECTIONS

Exact resolution of radar backscatter by tomographic methods is achievable only with the idealized δ -function model that was employed for the derivation of the medicine-radar analogy. Hence, the tomographic inversion formula is only an approximate procedure for reconstructing the two-dimensional radar distributions, when it combines the projections that are actually generated by a Chirp-diversity radar. These projections can be characterized as fuzzy radar-analogous projections.

An acceptable reconstruction can still be achieved, however. Barring practical constraints, this can be accomplished by employing a swept frequency bandwidth that is sufficient with respect to the desired resolution. An alternative, but less direct approach is by employing some type of restoration that will transform the fuzzy projections to more accurate tomographic projections.

Figures 21 and 22 provide some results concerning this issue. Figure 21 illustrates the point spread characteristic which was constructed with fuzzy projections. For this construction, the projection corresponding to a point distribution was convolved with $(\sin(x)/x)^2$. Conventional tomographic processing was then applied. The figure displays the point spread characteristic before and after affecting this transformation. Widening of the mainlobe is apparent.

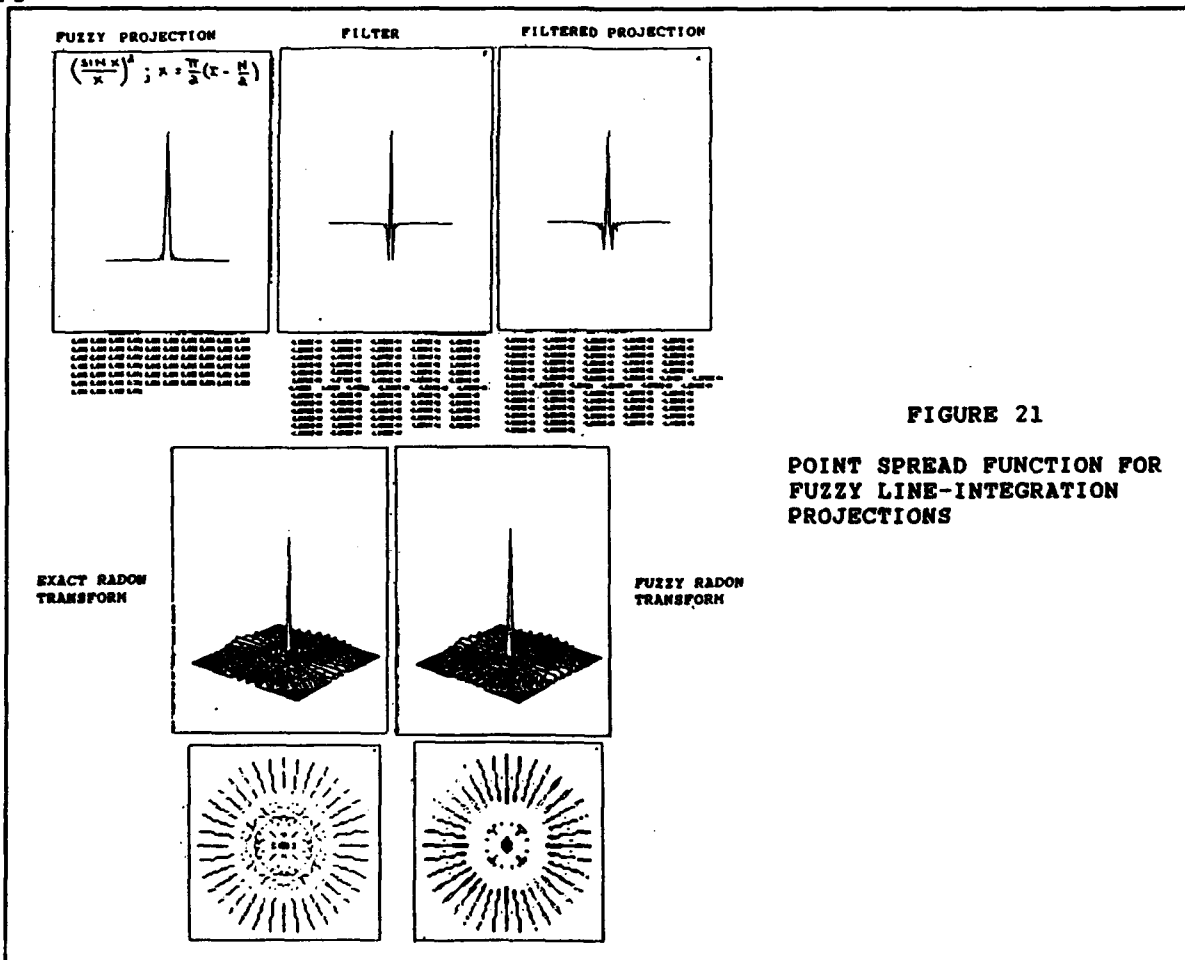


FIGURE 21

POINT SPREAD FUNCTION FOR FUZZY LINE-INTEGRATION PROJECTIONS

Figure 22 provides the tomographic reconstructions which were obtained, with exact and fuzzy projections, for a hemispheric distribution. Since this distribution is symmetrical, its projections are isotropic and ideally described by an ABEL transform

$$\frac{\pi}{2} R^2 (R^2 - x^2)$$

where R denotes its radius. For this experiment, the conventional filtering was modified. In lieu of the conventional filter, a filter was employed whose impulse response was equal to the filtered projection from the preceding case. Effectively, this modification of the filter had the same effect as computing the projections with fuzzy-line integrations. The effect is barely apparent. This, probably, is due to the nature of the distribution.

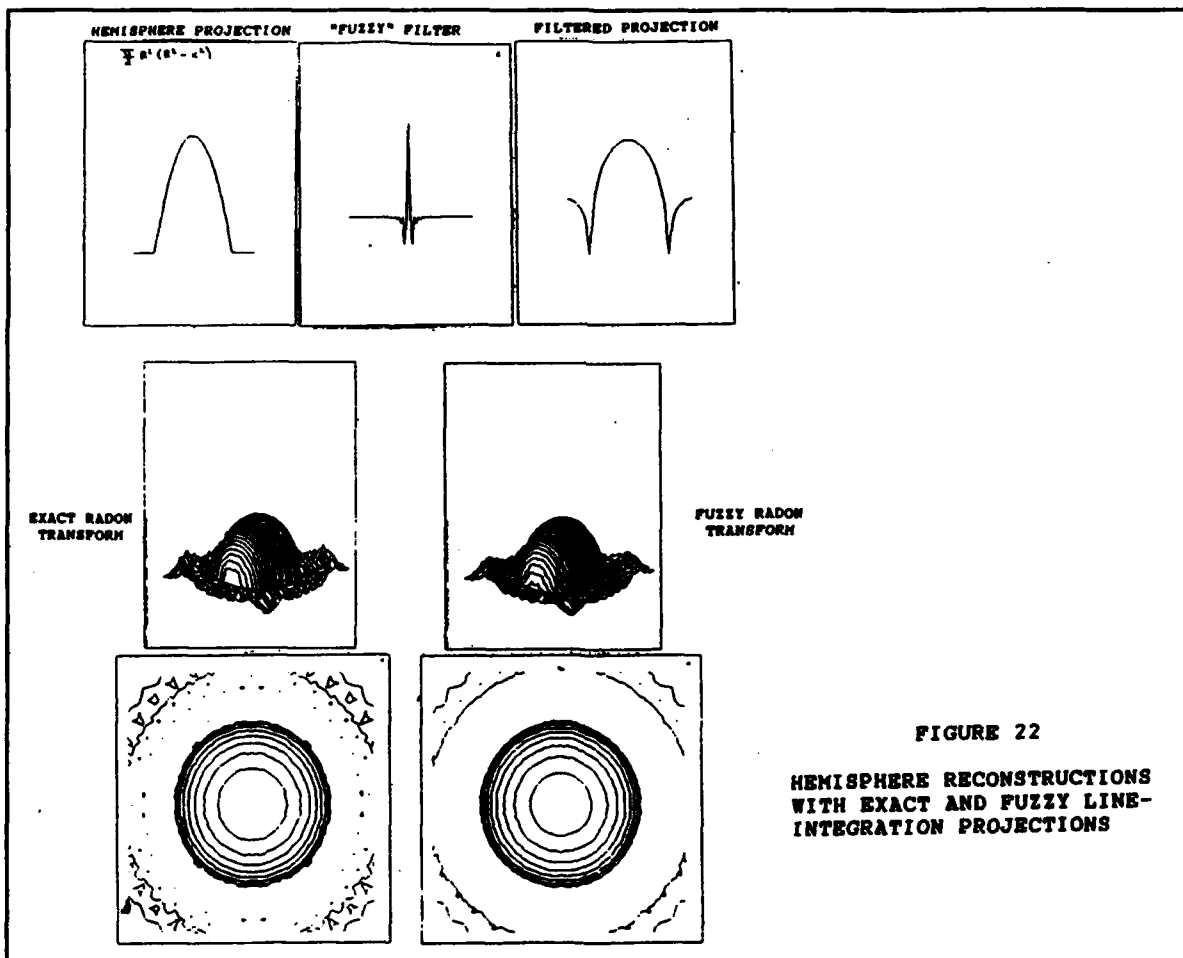


FIGURE 22
HEMISPHERE RECONSTRUCTIONS
WITH EXACT AND FUZZY LINE-
INTEGRATION PROJECTIONS

4.5 A PRIMITIVE TARGET MODEL

The rotating object is a classic radar target that has interested scientists as well as research and development engineers for many years. Since target features in crossrange coincide uniquely with Doppler shifts, the resolution of these features is accomplished with conventional coherent Doppler processing. The technique is called ISAR, short for inverse synthetic aperture radar. In conventional ISAR systems, the range-Doppler images are derived by illuminating the rotating target with a coherent sequence of wideband pulses, then processing the the pulsed echoes coherently; the generic implementation consists of a range-gated filter bank (see figure 24).

A primitive target model is described in this section, that has been employed to explain to others how this imaging task can also be accomplished by using tomographic methods. Referring to figure 23a, the model consists of a rotating ring. This is in the same plane as the radar and visible to it at every point around the circumference of the ring.

The distribution over the $r\phi$ -plane that this primitive model generates consists of an elliptic line-like distribution. The description of this ellipse in terms range and range rate is

$$(R - r)^2 + \left(\frac{\dot{R}}{\theta}\right)^2 = r^2$$

where R and \dot{R} denote range and range rate, respectively, and r denotes the radius of the ring, and θ is the rotation rate. This distribution is drawn in figure 23b.

For this distribution, the tomographic projections can be described by a mathematical formula that reflects the dependance on the particular viewing angle which is expressed as follows

$$\psi = \tan^{-1}\left\{\frac{\lambda}{c} (\text{Chirp rate})\right\}$$

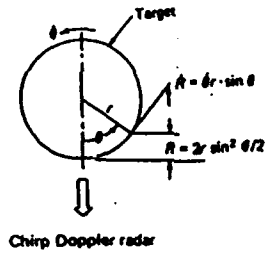
where λ and c , respectively, denote wavelength and the velocity of light. Hence, the functional form for the projections can be stated as follows.

$$p_{\psi}(l) = \frac{2r}{[Ar^2 - (AB - C)l^2]^{\frac{1}{2}}}$$

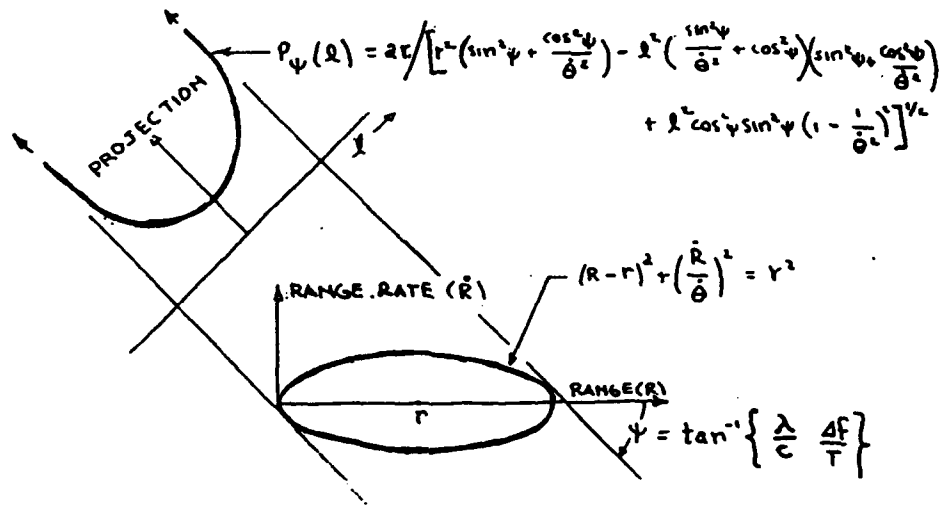
$$A = \sin^2 \psi + \frac{\cos^2 \psi}{\theta}, \quad B = \frac{\sin^2 \psi}{\theta} + \cos^2 \psi, \quad C = \left(1 - \frac{1}{\theta^2}\right) \cos^2 \psi \sin^2 \psi$$

An illustration of this is provided in figure 23b, while the tomographic reconstruction of the distribution, for a given set of the parameters r and θ , is shown in figure 23c.

(a) SYSTEM GEOMETRY



(b) THE RANGE(R)-RANGE RATE(\dot{R}) DISTRIBUTION AND A SAMPLE PROJECTION FOR ANGLE ψ



(c) RECONSTRUCTED RANGE(R)-RANGE RATE(\dot{R}) DISTRIBUTION

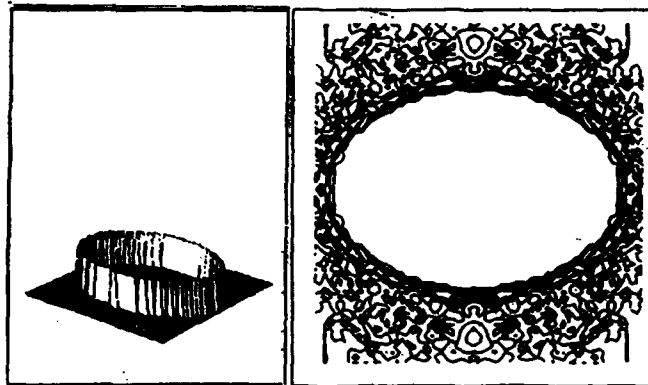


FIGURE 23 A PRIMITIVE EXAMPLE OF A TOMOGRAPHIC RECONSTRUCTION IN RADAR, IN WHICH A ROTATING RING-LIKE OBJECT IS THE TARGET .

5.0 COMPARISON OF TWO IMAGING APPROACHES

By exploiting coherent integration to process the pulses echoed back from some target, a conventional Doppler processing system (figure 24) will produce maximum gain in signal to noise and, theoretically, can achieve greater Doppler resolution by adding pulses to the pulse train that is transmitted. In spite of these seemingly superior attributes, the investigation of an alternative is justified because of the following situations.

1. Doppler as well as range delay are usually not constant. Normally, there is steady migration through resolution cells by the scattering points, particularly in the case of rotating targets. As a result, the effectiveness of the coherent integration diminishes as a function of time.

2. The coherent integration breeds multiple pop-up ambiguities that are characterized in the literature as a "Bed of Nails" (see figure 25) Bounded in range delay by the period between pulses and by the reciprocal of the period with respect to Doppler shift, the unambiguous area can never be enlarged. Unless the area to be imaged is similarly bounded, the ambiguities are manifested by aliasing artifacts superimposed on the images.

3. To derive the maximum performance that is offered by coherent integration, a rigid schedule of pulse transmissions is required. In a multipurpose system, this can conflict with other transmissions that also have to be scheduled.

By integrating the echoed pulses after detection, tomographic-based imaging offers ambiguity-free coverage which means no pop-up ambiguities across the entire domain of range delay and Doppler shift. In addition, the pulse transmissions can be scheduled independently which lessens the possibility of transmission conflicts in a multipurpose system. Also, the freedom to transmit pulses at any time can be utilized to achieve better snapshots of the range-Doppler distributions by speeding up the transmission of pulses as a stop action measure.

The table next page summarizes made above.

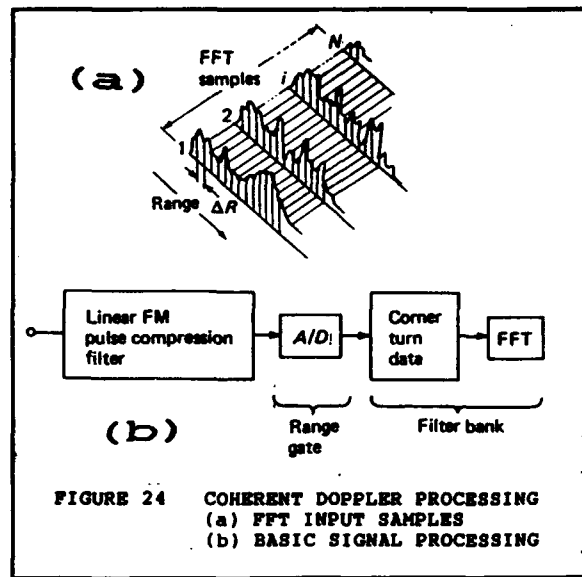


FIGURE 24 COHERENT DOPPLER PROCESSING
(a) FFT INPUT SAMPLES
(b) BASIC SIGNAL PROCESSING

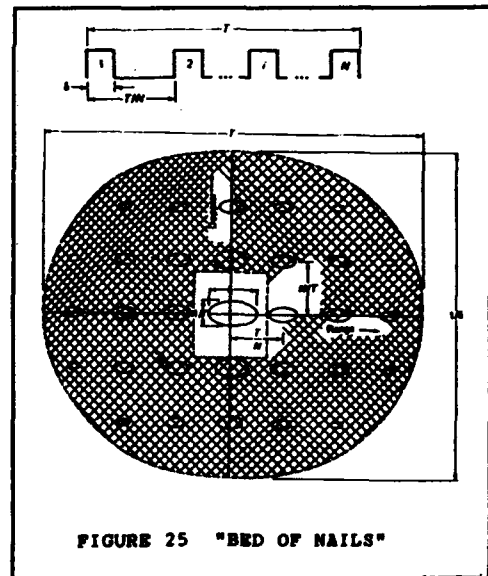


FIGURE 25 "BED OF NAILS"

COMPARISON OF TECHNIQUES

DESCRIPTION:

TECHNIQUE.....	PULSE DOPPLER RADAR	CHIRP DIVERSITY RADAR
STATUS.....	Conventional	New Idea
TRANSMIT.....	Wideband Pulse Train	Diverse Linear-FM Pulse Suite
RECEIVE.....	Pulse Compression & Coherent Doppler Integration	Pulse Compression & Noncoherent Tomographic Combining

ISSUES:

S/N..... GAIN	Maximum	< Maximum
AMBIGUITY..... CHARACTERISTIC	"BED OF NAILS"	SUPERTHUMBSTACK
EFFECTIVE..... INTEGRATION TIME	Limited due to target dynamics	Snapshot measurements offer unlimited diversity combining
PULSE..... TRANSMISSIONS	Ridgid pulse schedule	Independent pulses
PHASE..... COHERENCE	Intrapulse stability	Accurate interpulse FM rate

6.0 COMPUTATIONAL FRAMEWORK

To reconstruct a two-dimensional distribution for which measurements have provided the line-integral projections that constitute its Radon Transform, any one of three established tomographic computational procedures can be employed. These consist of the (1) the Inverse Radon Transform, (2) computations based on the Projection-Slice Theorem, and (3) an algebraic-based reconstruction. The reconstructions that have been produced during this study were derived by filtering the projections, then backprojecting the response. Since the filtering was done by appropriately weighting DFT amplitudes, these tomographic reconstructions were actually obtained by a combination of the procedures listed above as (1) and (2). This computational framework can also be employed for systems in which tomographic methods are combined with a Chirp diversity radar in order to map radar backscatter as a function of range and Doppler.

Figure 26 presents one possible system configuration. The Chirp diversity is provided in this system during a sequence of linear FM pulse transmissions. The receiver is shown with a common pulse compression network which is preceded by a mixing circuit. The two inputs consist of (1), the delayed echo with linear FM rate v_i , and (2), a reference pulse with a small increment, Ω , in the Chirp rate. The latter is delayed so that it coincides with a time delay corresponding to a reference range.

The mixing process produces an output pulse which is approximately the same duration as the input but with the linear FM rate reduced to Ω . The purpose is twofold: (1) the signal bandwidth is reduced for easier processing, and (2) the FM rate is normalized to enable the pulse compression with a common circuit.

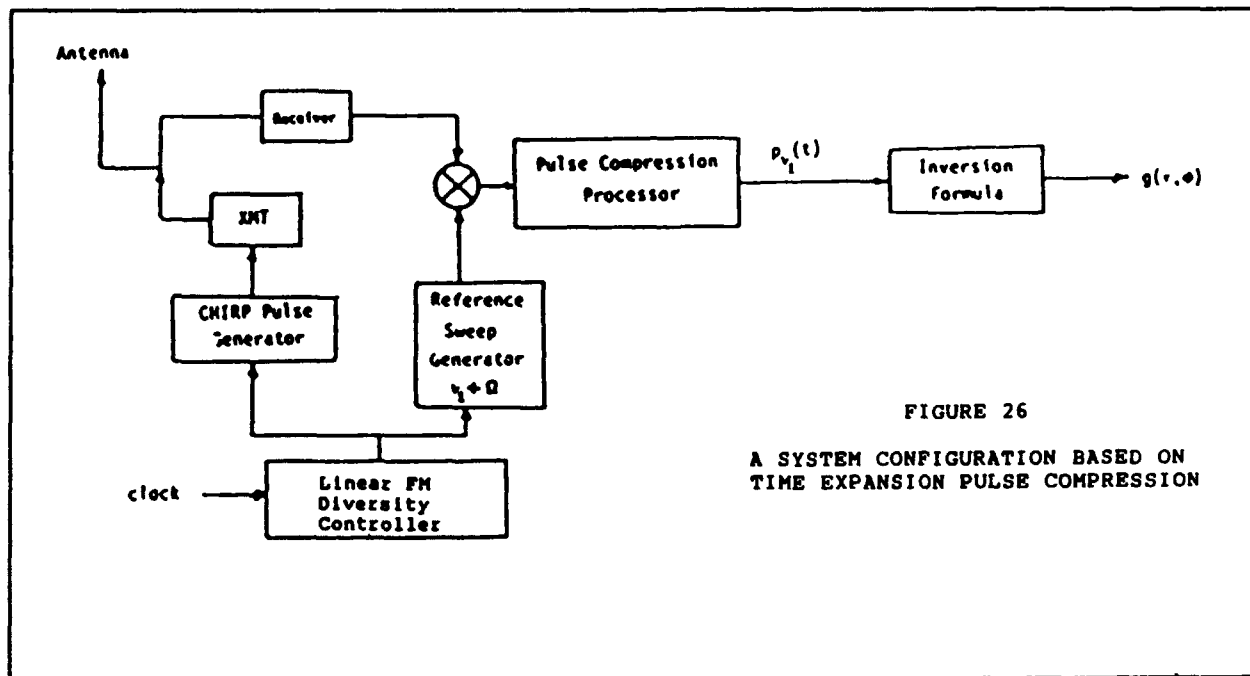


FIGURE 26

A SYSTEM CONFIGURATION BASED ON
TIME EXPANSION PULSE COMPRESSION

Although the bandwidth is reduced by the preceding processing scheme, resolution in range is not sacrificed. This is explained by considering the output time delay difference for two different input range displacements. Thus, the time delay difference at the output is scaled by the same factor that the output pulses are widened due to narrower pulse compression bandwidths. This scale factor equals the ratio of the original bandwidth divided by the bandwidth after the mixing. By maintaining the ratio of these bandwidths with every pulse transmission, pulse to pulse variations in output time scale are avoided; a constant time scale is required for inputs supplied to the tomographic processor.

The preceding "time expansion" system yields projections over range delay. However, analogous projections can also be produced over Doppler. These projection options are illustrated in figure 27 which also illustrates the linear-mapping transformation that arises as a result of the characteristic coupling of range delay and Doppler during Chirp pulse compression processing. The coordinate systems involved are: (1) range (R) and velocity (R), and (2), range delay (τ) and Doppler offset (ϕ).below.

Expressed in matrix format, the linear relationship between these coordinates is as follows.

$$\begin{bmatrix} \tau \\ \phi \end{bmatrix} = \begin{bmatrix} a_1 & a_2 \\ a_3 & a_4 \end{bmatrix} \begin{bmatrix} R \\ \dot{R} \end{bmatrix}$$

$$a_1 = \frac{2}{c}$$

$$a_2 = \left(\frac{2}{c}\right)\left(\frac{T}{\Delta f}\right)f_0$$

$$a_3 = -\left(\frac{2}{c}\right)\left(\frac{\Delta f}{T}\right)$$

$$a_4 = \left(\frac{2}{c}\right)f_0$$

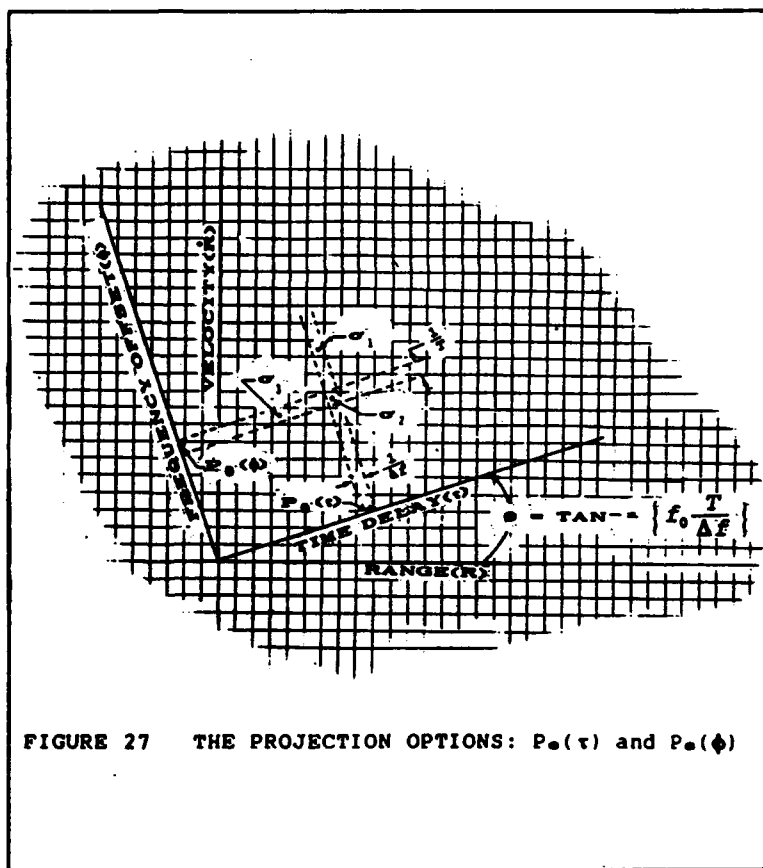


FIGURE 27 THE PROJECTION OPTIONS: P_a(τ) and P_a(ϕ)

Figure 27 displays a simple scenario consisting of three isolated backscatter sources with cross-sections σ_1 , σ_2 , and σ_3 . This is mapped, simultaneously, on the RR -plane and on the $\tau\phi$ -plane which is rotated by:

$$\theta = \text{TAN}^{-1} \left\{ \frac{a_2}{a_1} \right\}$$

$$= \text{TAN}^{-1} \left\{ f_0 \frac{T}{\Delta f} \right\}$$

The figure can be interpreted as follows. In general, the tomographic projections $P_\theta(\tau)$ and $P_\theta(\phi)$ are comprised of backscatter that accumulates in windows with alignments perpendicular to range delay and Doppler offset, respectively. The window sizes with respect to range delay and Doppler, respectively, are

$$(1) \quad \Delta\tau = \frac{1}{\Delta f}$$

$$(2) \quad \Delta\phi = \frac{1}{T}$$

For the particular case that is illustrated, both projections consist of a pair of dirac-like responses, while for the specific windows that are illustrated, the response amplitudes are

$$(1) \quad P_\theta(\tau) = \sigma_1 + \sigma_2$$

$$(2) \quad P_\theta(\phi) = \sigma_1 + \sigma_3$$

Some other Chirp rate and corresponding rotation of the $\tau\phi$ -plane will yield different projections.

As described above, the projections on τ , which are represented by $P_\theta(\tau)$, are available as outputs from a system such as in figure 27. To extract the analogous projections $P_\theta(\phi)$, it is necessary in effect to corner-turn the pulse compression processing. This can be done by (1), nulling the FM increment in the reference Chirp signal that is supplied to the mixer and (2), replacing the pulse compression circuit with some kind of spectrum analyser (eg., FFT or the Chirp Z Transform). The schematic for the revised system is provided in figure 28.

The system that is ultimately chosen to image backscatter distributed over range and Doppler can consist of either one of the configurations in figures 26 and 28. Another option is a configuration in which the tomographic computations are performed by combining the projections from both systems. A configuration such as this is attractive since it offers the same image quality with half as many Chirp transmissions.

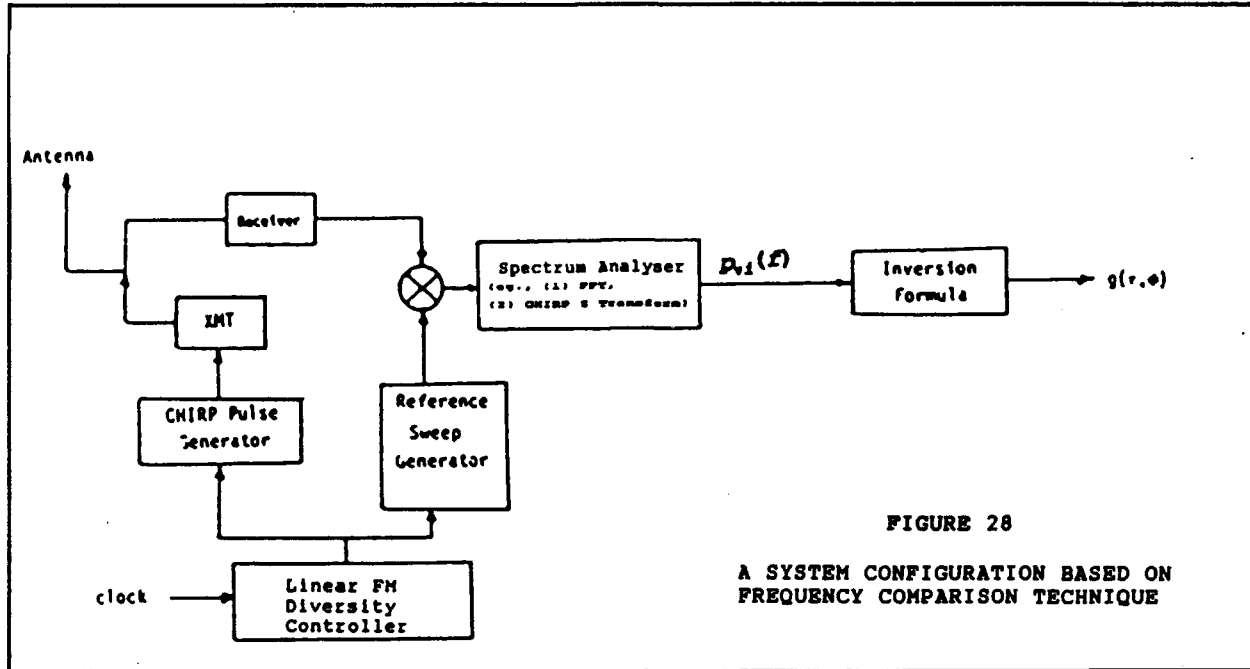


FIGURE 28

A SYSTEM CONFIGURATION BASED ON
FREQUENCY COMPARISON TECHNIQUE

7.0 CONCLUSION

The conceptual system for conventional mapping of radar echo intensities in range delay and Doppler shift coordinates consists of a bank of matched filters whose center frequencies are progressively offset with respect to the carrier frequency; the equivalent is a two-dimensional array of correlators for displacements in range delay as well as Doppler shift. The maps that are produced are never exact, however. This condition is a symptom of the point spreading which is characterized by the radar ambiguity function. The point spreading, an inescapable law of nature, is the penalty which is paid because the view of objects is always through windows hence the information available for conventional imaging is always incomplete. Lord Rayleigh recognized this fact and, thereupon, provided his well-known resolution criterion which quantifies our inability to see things as they really are.

Although optimization is theoretically available to the designer who can specify idealized waveforms, he ultimately must accommodate certain constraints as well as conflicting system requirements that limit how much can be achieved in practice.

The practical solution, up until now, has been to combine the echoes returned to radar corresponding to a sequence of coherent pulse transmissions. These transmissions are often encoded by internal modulation so as to enable pulse compression when the echoes are received. The system is referred as pulse Doppler, and the corresponding point spread function is commonly characterized as a "bed of nails".

This pulse Doppler solution normally only provides access to the central region of the ambiguity plane. The boundaries are established by the pulse repetition frequency (PRF) in one direction and by the period between the pulses in the other dimension. Any echo intensity from a source outside this region is folded back onto the central region. This fold-back intensity cannot be distinguished from true distribution of intensity and is commonly termed "aliasing".

A serious attempt is usually made during system design to limit the amount of aliasing that can occur. Idealistically, the central region is made sufficiently large so that no intensity distribution extends beyond the boundaries. This goal is often elusive, however. The reason being the reciprocal coupling that exists between the PRF and the pulse period, which bars simultaneous enlargement of both dimensions of the central region. For many situations, therefore, the mapping accuracy will depend on the final compromise that is acceptable -- all things considered.

The likelihood for such situations as above arising during the design of the conventional system can be expected to grow in the future. This will be driven by a requirement for higher carrier frequencies to accommodate the wider pulse compression bandwidths that will be necessary to meet expected demands for greater range resolution. For a range resolution of less than one foot, it will be necessary to employ millimeter wave transmissions to mitigate the spectrum distortion at the low end due to fold-over. The unambiguous detection area will shrink, as a result, due to greater Doppler-velocity sensitivity. A compounding of this dilemma can

occur if a greater unambiguous detection range is also demanded which will require a longer pulse period. The probability that there will be faster targets in the future, further intensifies the likelihood their images will be ambiguous.

By integrating the echoed pulses after detection, a Chirp diversity radar incorporating tomographic methods possesses none of ~~these~~ ^{the} symptoms associated with conventional pulse Doppler techniques. The point spreading is a thumbtack-like function.

Thus, range-Doppler coverage is unlimited since there are no ambiguity pop-ups to restrict this coverage. In addition, it appears that the mainlobe width depends exclusively on bandwidth. In contrast, the classic thumbtack ambiguity function ~~shown in figure 7~~ is affected both by bandwidth and, inversely, by the integration time. More important than the preceding discovery is the property that ambiguity function is not constrained by radar uncertainty principles. Hence, "the sands of the beach" is not a suitable analogy to describe this ambiguity function. It is concluded that this superthumbtack characteristic offers superior resolution for an accurate interpretation of radar backscatter with respect to detection, parameter estimates, and imaging.

An added benefit by integrating the echoed pulses after detection is the freedom to schedule pulse transmissions independently. The advantages gained as a result, over conventional imaging techniques, are the following. First, the freedom to transmit pulses at any time enables accelerated measurements which can yield images with stop-action sharpness. Second, since the pulse transmissions are not constrained to a rigid PRF schedule, they can be interleaved with other transmissions in a multifunction radar so as to utilize available energy in the most efficient manner.

The radar applications in which the Chirp diversity combined with tomography can be employed are many. In general, this covers all of the categories where range and Doppler information is utilized. Some examples are ICBM wake classification, surveillance and tracking, weather mapping and microburst detection, traffic control, ionospheric sounding, radar astronomy, and imaging rotating targets. The value of this technique will become significant when it is no longer possible to exploit coherent techniques effectively. The environment for this to unfold will occur perhaps in a future SDI scenario or possibly in probing outer space for menacing objects. Laser radars operating at optical frequencies are particularly vulnerable regarding ambiguous Doppler, while potentially high target speeds compared acoustic propagation velocity makes sonar similarly vulnerable. It is predicted that this application of tomography will eventually become the principal radar approach for mapping radar backscatter as a function range and Doppler shift.

8.0 REFERENCES

- [1] **R. GORDON, G.T. HERMAN, S.A. JOHNSON**, *Image Reconstruction From Projections*, *Sci. American*, (1975), Oct., 56-66
- [2] **R.N. BRACEWELL**, *Strip Integration in Radio Astronomy*, *Aust. J. Phys.*, 9(1956), 198-217.
- [3] **K.A. DINES AND R.J. LYTLE**, *Computerized Geophysical Tomography*, *Pro. IEEE*, 67(1979), 1065-1073.
- [4] **R.A. CROWTHER, D.J. DeROSIER, AND, A. KLUG**, *The reconstruction of a three dimensional structure from projections and its application to electron microscopy*, *Pro. Roy Soc. London*, A317(1970), 319-340.
- [5] **P. REIMERS AND J. GOEBELS**, *New Possibilities of Nondestructive Evaluation By X-RAY Computed Tomography*, *Materials Evaluation*, 41(1983), 732-737.
- [6] **D.C MUNSON, Jr., J.D. O'BRIEN, AND, W.K.JENKINS**, *A Tomographic Formulation o Spotlight-Mode Synthetic Aperture Radar*, *Pro. IEEE*, 71(1983), 917-925.
- [7] **D.L. MENSA, S. HALEVY, G. WADE**, *Coherent Doppler Tomography for Microwave Imaging*, *Pro. IEEE*, 71(1983), 254-261
- [8] **M. BERNFELD**, *CHIRP Doppler Radar*, *Pro. IEEE*, 72(1984), 540-541.
- [9] **E. FEIG AND A. GRUNBAUM**, *Tomographic Methods in Range-Doppler Radar*, *Inverse Problems*, 2(1986).
- [10] **P.M. WOODWARD**, *Probability and Information Theory With Applications to Radar*, Pergamon Press(1953).
- [11] **C.E. COOK AND M. BERNFELD**, *Radar Signals, An Introduction to Theory and Application*, Academic Press(1967).
- [12] **H.L. VAN TREES**, *Detection, Estimation, and Modulation Theory, Part III*, page 452, John Wiley & Sons, Inc. (1969),
- [13] **S.R. DEANS**, *The Radon Transform and Some of Its Applications*, John Wiley & Sons, INC. (1983)
- [14] **R.A. BROOKS, G.H. GLOVER, A.J. TALBERT, R.L. EISENER, and F.A. DiBIANCA**, *Aliasing: A Source of Streaks in Computed Tomograms*, *J. Computer Assisted Tomography*, 3(1979), 511-518.

APPENDIX A

A TEST AND DEMONSTRATION CONFIGURATION

I. RAYTHEON FACILITIES

Raytheon Company at Sudbury and Wayland, Massachusetts currently maintains several facilities for testing microwave, millimeter-wave, and laser radars. They are conveniently placed in laboratories inside the plant as well as on surrounding grounds, and are regularly utilized for research and development in connection with new antenna system designs design as well as for predicting the radar cross-section of different targets. Effective utilization of these facilities is ensured by resident teams consisting of qualified microwave engineers and technicians. In addition, the instrumentation equipment permanently installed at each facility, consisting of sophisticated microwave measuring devices as well as computers, also ensures precise measurements and a rapid reduction the data to useful information.

Any of these facilities offers a testing environment that is suitable for controlled experiments which can demonstrate the capability tomographic imaging. But there may be similar facilities not owned by Raytheon Company which will require less costly developments in order to implement a test and demonstration program. An investigation of the possibility is certainly worth considering.

II. SIGNAL PROCESSING FUNCTIONS

The functional diagram for a possible test configuration is illustrated in figure A₁. Functions are divided between tasks performed with a computer and various signal processing tasks. The former consist of tomographic computations and also computations which will produce a suite of linear FM waveforms with different chirp rates. By incorporating a provision for transporting digitized signals via magnetic tape, these computations can be performed off-site. This will enable ongoing analyses to continue at the workstation, without an interruption in order to relocate the computer to the test site.

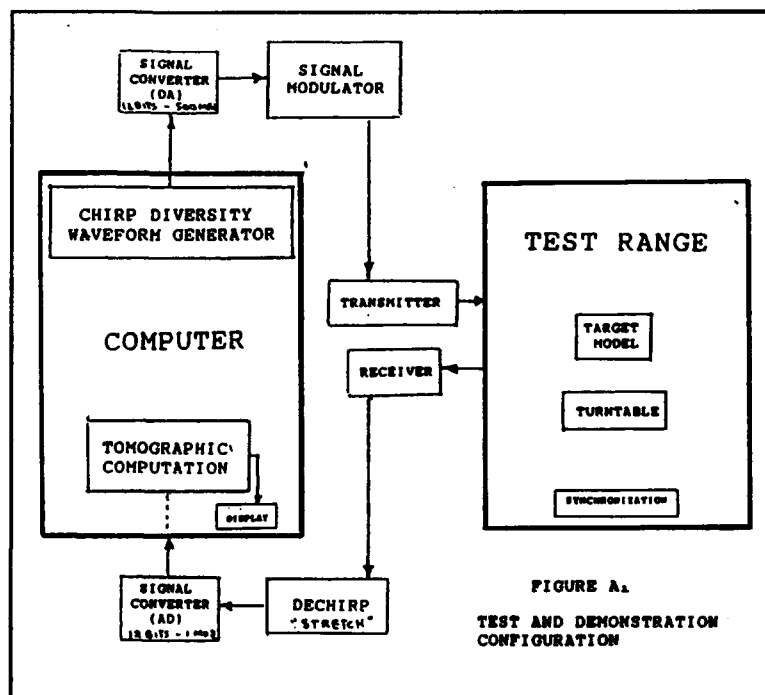


FIGURE A₁
TEST AND DEMONSTRATION
CONFIGURATION

To buffer the digitized signals, a RAM memory

will be installed at the test site with sufficient capacity to store input-output data for one radar transmission. It will be necessary for this digital memory to provide a buffer for high speed (500 MHZ bandwidth) output data as well as for relatively narrow bandwidth data of less than 500 KHZ.

The wideband output data will consist of (12 bit) I and Q digital samples that are transported from the computer via magnetic tape. Representing one chirp modulation pulse, this data will be output to a D/A, then channeled to a single sideband modulator and, subsequently, supplied as input to a (60 MHZ) microwave transmitter.

The narrow bandwidth input data will consist digitized (12 bit) I and Q samples representing 'stretch' processed radar echoes for a single chirp transmission. (The 'stretch processing is a familiar technique whereby the echoes are dechirped by mixing them with a an undelayed replica of the signal transmitted).

III. TRANSMIT/RECEIVE CONFIGURATION

Separate transmit and receive horns are required. This requirement arises because their signals overlap and must therefore be isolated. The horns will be elevated to an altitude of 60 feet and made to face downward to a rotating platform on the ground at approximately 134 feet radar range (figure A₂). A similar installation has been employed at the Environmental Research Institute of Michigan for studies concerning SAR and ISAR signal processing [*]. The specification here is that the platform have 20 feet diameter and be able to rotate at a maximum rate of 30 RPM. This will provide a maximum Doppler shift of several kilohertz after compensation for the oblique intercept angle. (The maximum Doppler shift should be sufficient for the experiments that are to be performed.) Adequate platform stabilization is required with respect to speed as well as transverse motion, which will limit spurious Doppler spreading to a maximum of 100 HZ.

IV. HORN DESIGN

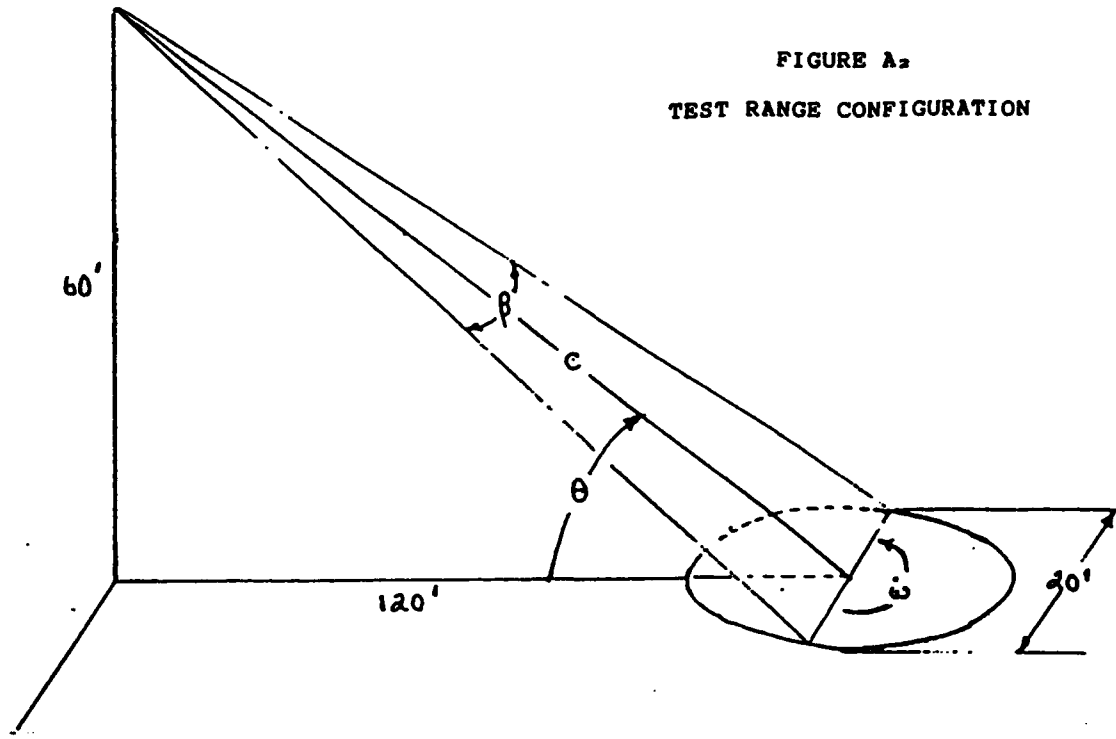
The design of the horns for transmitting and receiving will provide radiation beams that will cover the entire surface area of the rotating platform. Approximate horn dimensions required for this at 0.5 cm (60 GHZ) wavelength are as follows:

Length	=	15	cm
H Plane Aperture	=	5	cm
E Plane Aperture	=	4.34	cm

V. TRANSMITTER POWER

To provide 20 DB echoes relative to noise, for a 6 square centimeter RCS mounted on the rotating platform target requires 15 mw peak power. This is based on 27 DB gain computed for the horns and assumes 41.7 DB pulse compression gain is obtained by transmitting a 30 us pulse that is frequency swept over a bandwidth of 500 MHZ. This is a maximum requirement, since the peak power requirement will drop, assuming constant bandwidth, as the pulse duration is increased to acquire lower FM slopes for full angle coverage regarding tomographic projection aspects.

FIGURE A₂
TEST RANGE CONFIGURATION



- | | |
|-------------------------------|--|
| a. TARGET MODEL | (1) Point Target (6 cm ² RCS) |
| | (2) Multiple Point Targets
(various RCS per target) |
| | (3) Ring Target |
| b. WAVELENGTH | Millimeter-wave (60-100 GHZ) |
| c. XMT POWER | 15mw for 20 DB S/N |
| d. MODULATION | Chirp Diversity |
| e. SWEPT BANDWIDTH | 500 MHZ (nominal) |
| f. FM RATE | +/- megahertz per μs |
| | Long CW Pulse |
| | 0.10 |
| | ⋮ |
| | 6.50 |
| | Short CW Pulse |
| g. SIGNAL PROCESSING | "Stretch" Pulse Compression |
| h. TOMOGRAPHIC ALGORITHM..... | Filtered Backprojection |
| i. PLATFORM: (1) SPEED | 1/2 rps |
| (2) STABILITY... | 100 HZ |

[*] J.L. WALKER, *Range-Doppler Imaging of Rotating Objects*,
Dissertation for D. Phil., U. of Michigan, (1974)